SANDIA REPORT
SAND2006-6889
Unlimited Release
Printed Novemeber 2006

Micropolarizing Device for Long Wavelength Infrared Polarization Imaging

Shanalyn A. Kemme, Alvaro A. Cruz-Cabrera, Robert R. Boye, Tony Carter, Sally Samora, Chuck Alford, Joel R. Wendt, Gregory A. Vawter, Jody L. Smith

Prepared by
Sandia National Laboratories
Albuquerque, New Mexico 87185 and Livermore, California 94550

Sandia is a multiprogram laboratory operated by Sandia Corporation,
a Lockheed Martin Company, for the United States Department of Energy's
National Nuclear Security Administration under Contract DE-AC04-94AL85000.

Approved for public release; further dissemination unlimited.

Issued by Sandia National Laboratories, operated for the United States Department of Energy by Sandia Corporation.

NOTICE: This report was prepared as an account of work sponsored by an agency of the United States Government. Neither the United States Government, nor any agency thereof, nor any of their employees, nor any of their contractors, subcontractors, or their employees, make any warranty, express or implied, or assume any legal liability or responsibility for the accuracy, completeness, or usefulness of any information, apparatus, product, or process disclosed, or represent that its use would not infringe privately owned rights. Reference herein to any specific commercial product, process, or service by trade name, trademark, manufacturer, or otherwise, does not necessarily constitute or imply its endorsement, recommendation, or favoring by the United States Government, any agency thereof, or any of their contractors or subcontractors. The views and opinions expressed herein do not necessarily state or reflect those of the United States Government, any agency thereof, or any of their contractors.

Printed in the United States of America. This report has been reproduced directly from the best available copy.

Available to DOE and DOE contractors from
U.S. Department of Energy
Office of Scientific and Technical Information
P.O. Box 62
Oak Ridge, TN 37831

Telephone: (865) 576-8401
Facsimile: (865) 576-5728
E-Mail: reports@adonis.osti.gov
Online ordering: http://www.osti.gov/bridge

Available to the public from
U.S. Department of Commerce
National Technical Information Service
5285 Port Royal Rd.
Springfield, VA 22161

Telephone: (800) 553-6847
Facsimile: (703) 605-6900
E-Mail: orders@ntis.fedworld.gov
Online order: http://www.ntis.gov/help/ordermethods.asp?loc=7-4-0#online

SAND2006-6889
Unlimited Release
Printed Novemeber 2006

Micropolarizing Device for Long Wavelength Infrared Polarization Imaging

LDRD 79867 Final Report

Shanalyn A. Kemme, Alvaro A. Cruz-Cabrera, Robert R. Boye, Tony Carter, Sally Samora, Joel R. Wendt
Photonic Microsystems Technologies

Chuck Alford, Gregory A. Vawter
RF Microsystems Technologies

Jody L. Smith
Remote Sensing & Exploitation

Sandia National Laboratories
P.O. Box 5800 M/S 1082
Albuquerque, NM 97185-1082

Abstract

The goal of this project is to fabricate a four-state pixelated subwavelength optical device that enables mid-wave infrared (MWIR) or long-wave infrared (LWIR) snapshot polarimetric imaging. The polarization information can help to classify imaged materials and identify objects of interest for numerous remote sensing and military applications.

While traditional, sequential polarimetric imaging produces scenes with polarization information through a series of assembled images, snapshot polarimetric imaging collects the spatial distribution of all four Stokes' parameters simultaneously. In this way any noise due to scene movement from one frame to the next is eliminated.

We fabricated several arrays of subwavelength components for MWIR polarization imaging applications. Each pixel unit of the array consists of four elements. These elements are micropolarizers with three or four different polarizing axis orientations. The fourth element sometimes has a micro birefringent waveplate on the top of one of the micropolarizers. The

linear micropolarizers were fabricated by patterning nano-scale metallic grids on a transparent substrate. A large area birefringent waveplate was fabricated by deeply etching a subwavelength structure into a dielectric substrate. The principle of making linear micropolarizers for long wavelengths is based upon strong anisotropic absorption of light in the nano-metallic grid structures. The nano-metallic grid structures are patterned with different orientations; therefore, the micropolarizers have different polarization axes. The birefringent waveplate is a deeply etched dielectric one-dimensional subwavelength grating; therefore two orthogonally polarized waves have different phase delays. Finally, in this project, we investigated the near field and diffractive effects of the subwavelength element apertures upon detection.

The fabricated pixelated polarizers had a measured extinction ratios larger than 100:1 for pixel sizes in the order of 15 μm by 15 μm that exceed by 7 times previously reported devices.

The fabricated birefringent diffractive waveplates had a total variation of phase delay rms of 9.41 degrees with an average delay of 80.6 degrees across the MWIR spectral region.

We found that diffraction effects change the requirement for separation between focal plane arrays (FPA) micropolarizer arrays and birefringent waveplates arrays, originally in the order of hundreds of microns (which are the typical substrate thickness) to a few microns or less. This new requirement leads us to propose new approaches to fabricate these devices.

Contents

Figures

Tables

Introduction

There is interest in capturing and storing polarization images in the mid wave infrared (MWIR), similar to the ways intensity information is taken using a pixelated focal plane array (FPA). Several techniques have been proposed including the use of rotating polarizers[1,2], rotating waveplates[3,4], or a snapshot[5,6,7] that measures three or four Stokes parameters in a single frame. The first and the second methods have limitations in speed due to the need to take several images sequentially to get each linear polarization and the retardance component.

Polarimetric imaging measures the polarization states of light from all the points of the scene. Figure 1 shows three polarization states of completely polarized lights. The polarization state of light can be completely described by four Stokes parameters. The first Stokes parameter, S_0, represents the total optical intensity. The second Stokes parameter, S_1, represents the preference of the recorded optical signal for horizontal polarization versus vertical polarization. The third Stokes parameter, S_2, represents the preference of the recorded optical signal for linear polarization oriented along 45° versus 135° measured with respect to the horizontal direction. The fourth Stokes parameter, S_3, represents the preference for right-circular polarization versus left-circular polarization.

Previously, snapshot polarimetry[8,9] had limited resolution given large pixel size and small count in earlier FPAs. Since almost all the photodetectors available now are polarization insensitive, a combination of polarizing elements and photodetectors is needed to measure the polarization content of light. To obtain the complete Stokes vector, four independent measurements are necessary. If the two-dimensional scene is divided into N pixels, overall 4xN measurements are needed to obtain the complete polarimetric image. Thus, snapshot polarimetry becomes practical for FPAs with 20 μm pixels and pixel counts of 1024 x 1024.

The Stokes parameters[5,10] can be defined for a quasimonochromatic light propagating along the z-axis in equation (1):

$$\begin{aligned} S_0 &= \left\langle a_x^2 \right\rangle + \left\langle a_y^2 \right\rangle \\ S_1 &= \left\langle a_x^2 \right\rangle - \left\langle a_y^2 \right\rangle \\ S_2 &= 2 \cdot \left\langle a_x a_y \cos(\phi_x - \phi_y) \right\rangle \\ S_3 &= 2 \cdot \left\langle a_x a_y \sin(\phi_x - \phi_y) \right\rangle \end{aligned} \tag{1}$$

Where a_x and a_y are the instantaneous magnitude of the two orthogonal components E_x and E_y of the quasimonochromatic light wave, and ϕ_x and ϕ_y are their respective phase. E_x and E_y are defined in equation (2):

$$\begin{aligned} E_x(t) &= a_x(t) \exp\left[i(\phi_x(t) - 2\pi\nu t)\right] \\ E_y(t) &= a_y(t) \exp\left[i(\phi_x(t) - 2\pi\nu t)\right] \end{aligned} \tag{2}$$

ν is the mean frequency. The light that passes through a linear polarizer with electric vector aligned in the θ direction and delayed by ε after passing a phase retarding device is defined in equation (3):

$$E(t;\theta,\varepsilon) = E_x(t)\cos(\theta) + E_y(t)\exp(i\varepsilon)\sin(\theta) \tag{3}$$

And the irradiance is expressed by equation (4):

$$I(t;\theta,\varepsilon) = \left\langle E(t;\theta,\varepsilon)\cdot E^*(t;\theta,\varepsilon)\right\rangle \tag{4}$$

The four Stokes parameters are obtained by measuring the transmitted signals through three micropolarizers aligned in different orientations and the optical signal through a quarter waveplate and a micropolarizer. It can been shown that if we measure *I(0°,0), I(90°,0), I(45°,0) and I(45°, π/2)* the four Stokes parameters can be obtained from the measured optical signals as in equation (5):

$$\begin{aligned} S_0 &= I(0°,0) + I(90°,0) \\ S_1 &= I(0°,0) - I(90°,0) \\ S_2 &= 2\cdot I(45°,0) - I(0°,0) - I(90°,0) \\ S_3 &= 2\cdot I(45°,\frac{\pi}{2}) - I(0°,0) - I(90°,0) \end{aligned} \tag{5}$$

Where *I(0°,0)* is the optical irradiance through a linear polarizer oriented along the x-axis. *I(90°,0)* is the optical transmitted power through a linear polarizer oriented along the y-axis. *I(45°,0)* is the irradiance for a linear polarizer oriented 45 degree with respect to the x-axis, and *I(45°, π/2)* is the transmitted power transmitted through a quarter-wave plate and then a linear polarizer oriented 45 degree with respect to the x-axis.

Micropolarizers for long-wave infrared are made by patterning nano-scale metallic grids on a transparent substrate. The micro phase retarder is made by deeply etching the nano-scale dielectric structure on another substrate. H. Hertz[11] demonstrated for the first time a linear polarizer using metallic wires for radio frequency electromagnetic waves. The principle of using a metallic grid as an infrared polarizer is based on strong anisotropic absorption of light in the subwavelength metallic grid structures. The electric field parallel to the lines of the metal is absorbed because of the zero electric field inside the metal and the tangent boundary conditions. The electric field perpendicular to the lines of the metal is less absorbed in the metallic grid structure. In order to make a good metal grid polarizer, the period of the metallic grid must be at least one order of magnitude less than the incident wavelength. For mid-wave infrared (MWIR), the metallic structure feature size should be in the order of a couple hundreds of nanometers.

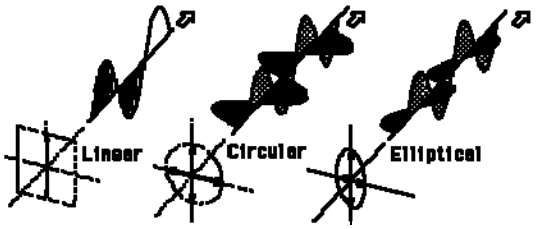

Figure 1. Electric and magnetic fields of polarized radiations.

Birefringent form waveplates are one dimensional subwavelength gratings etched into a substrate lead to an effective refractive index that is dependent on the incident polarization. A TE wave will interact with material boundaries parallel to the electric field while a TM wave has its magnetic field parallel to these boundaries. The different geometries lead to slight differences in the effective index for each polarization. This "form birefringence" effect[10] can be utilized to create polarization components such as waveplates.

1. Wiregrid Polarizer

1.1 Wiregrid Polarizer Design Space

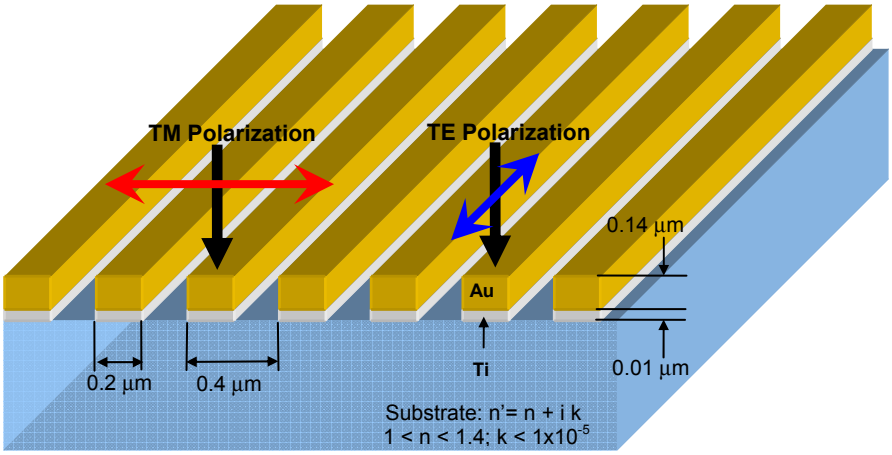

Figure 1.1 Illustration of a gold wire grid polarizer in a substrate with low refractive index values for n and k and the different parameters involved in designing of the device.

The overall goal of this part of the LDRD is to model, design and fabricate wire grid micro-polarizer arrays while varying their aperture dimensions to understand how their performance is affected by diffraction and near-field effects. The first aspect of the project entails the selection of materials that would work on the 2 to 5 µm regime. Gold is used as the metal for the wiregrid since it is a near ideal metal, for this application. The substrate must have low losses at the incident wavelengths (i.e. low imaginary part of the refractive index) and the real part of the refractive index must be low. A suspended gold subwavelength wire grid in air would be ideal, but it is mechanically inpractical to fabricate such long and thin wires. We have chosen a low refractive index substrate to support the gold subwavelength-period wire grid. The configuration is shown in Figure 1.1.

A numerical survey of the transmission of TM and TE fields was done for various wire grid period, metal thicknesses, substrate materials and wavelengths using rigorous couple wave analysis[12] (RCWA), as in Figure 1.2. The purpose of this mapping is to find dimensional and working spaces where the transmitted TM / TE extinction ratio is larger than 100:1 nominally and the TM transmission value exceeds 80%.

Mapping the design space for fused silica (SiO_2) substrates showed it was found that it could perform well between 2 and 3.5 µm, see Figure 1.2 (a), for the transmitted extinction ratio versus wire grid periods and gold thickness. The device has good transmission of the TM polarization up to λ= 3.5 µm as in Figure 1.2 (b); however, the transmission of the TM polarization for λ= 4 µm will be less than 80% as in Figure 1.2 (c). SiO_2 refractive index at 4 µm is 1.40 but the imaginary values, k, is significant at $5x10^{-5}$.

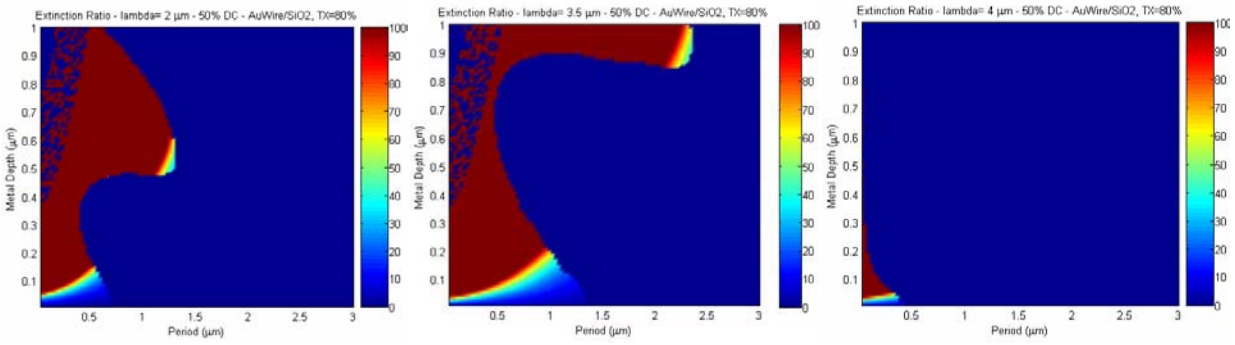

(a) (b) (c)

Figure 1.2 Simulation results for the TM/TE transmitted extinction ratio for a wiregrid polarizer made of gold on a fused silica substrate for the incident wavelengths of (a) λ= 2 µm, (b) λ= 3.5 µm and (c) λ= 4.0 µm. The graph shows the relationship between the period of the wiregrid (x-axis) and the thickness of the gold (y-axis). The TM intensity is threshold at 80% and any deep red zone in the graph has a desirable extinction ratio larger than 100:1. Notice the small working area (deep red) for λ= 4 µm because SiO_2 is absorptive beyond λ= 3.5 µm.

We searched for another material that is not absorptive between 2 and 5 µm (extremely low k value) and a low real part of the refractive index. Lithium Fluoride (LiF) has the real part of the refractive index varying from 1.37 to 1.32 and an imaginary, k, value that ranges from $2x10^{-12}$ to $2x10^{-6}$. From the simulations in Figure 1.3, we decided to fabricate parts with periods of 0.4 µm, Au thicknesses of 0.15 µm, and Ti thickness of 0.01 µm.

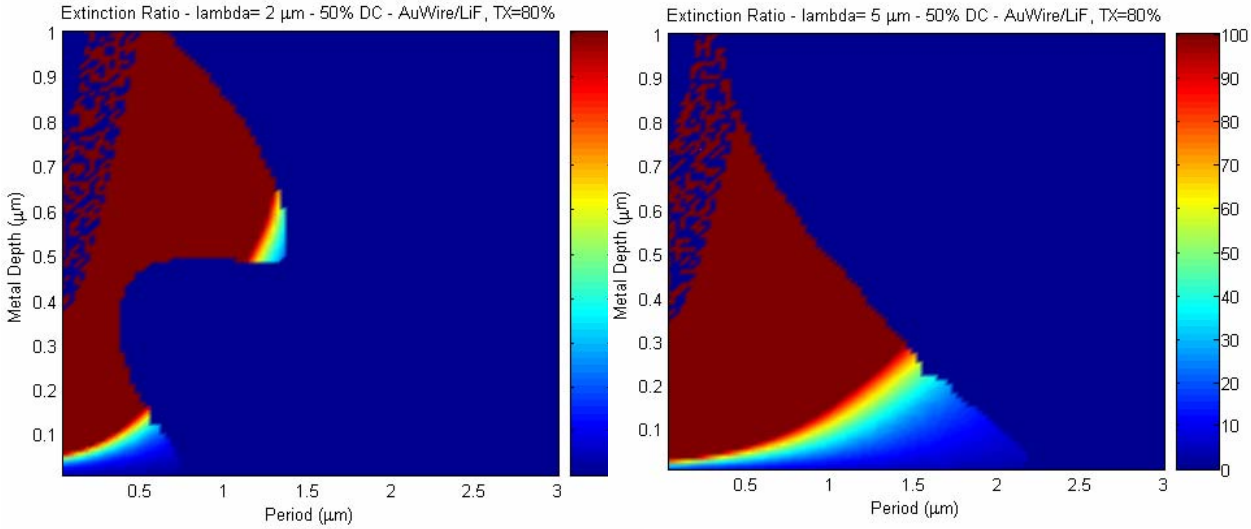

(a) (b)

Figure 1.3 Simulation results for the TM/TE transmitted extinction ratio for a wiregrid polarizer made of gold on a lithium fluoride substrate for incident wavelengths of (a) λ= 2 µm and (b) λ= 5 µm. The graphs show the relationship between the period of the wiregrid (x-axis) and the thickness of the gold (y-axis). The TM intensity is thresholded at 80% and any deep red zone in the graph has a desirable extinction ratio larger than 100:1. Notice the large deep red area for λ= 5 µm sdince lithium fluoride is not absorptive at this wavelength.

1.2 Fused Silica Devices - First Iteration

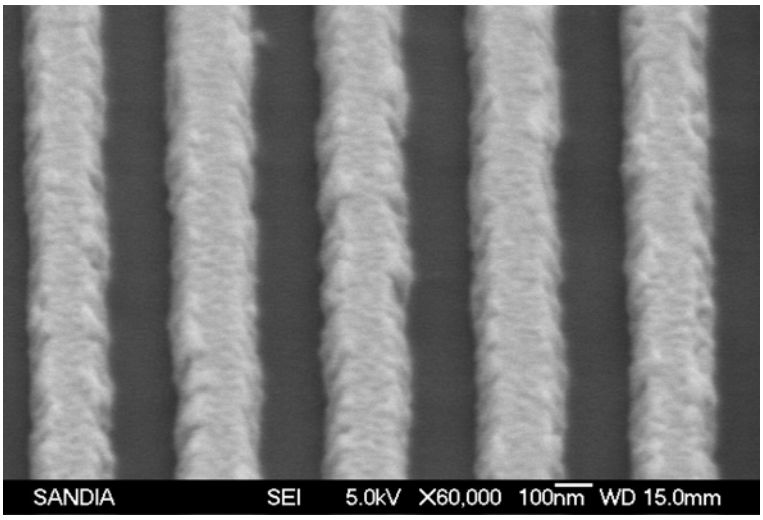

Figure 1.4 SEM image of the 56% duty cycle of gold wiregrid polarizer on fused silica

While waiting for the delivery of the LiF substrates, we fabricated parts in SiO_2 and tested them between 2 and 3.5 µm using the same design as the one intended for the LiF. This design still meets the extinction ratio of 100:1 and the 80% transmission of the TM polarization. The duty cycle for the design is ideally 50% (0.2 µm line). We fabricated three variations of the duty cycle to account for process shifts: 44%, 50% and 56% (0.176, 0.2 and 0.224 µm lines).

A coat of polymethyl methacrylate (PMMA) with a thickness of 0.3 µm is spun on top of a fused silica substrate and the PMMA is exposed with 0.2 µm lines by an e-beam writer and developed away. Titanium and gold are deposited on top of the patterned PMMA for subsequent lift-off, where the 0.01 µm of Ti acts as an adhesion layer for the 0.15 µm gold layer on fused silica. These initial devices had an area of 5 mm X 5 mm.

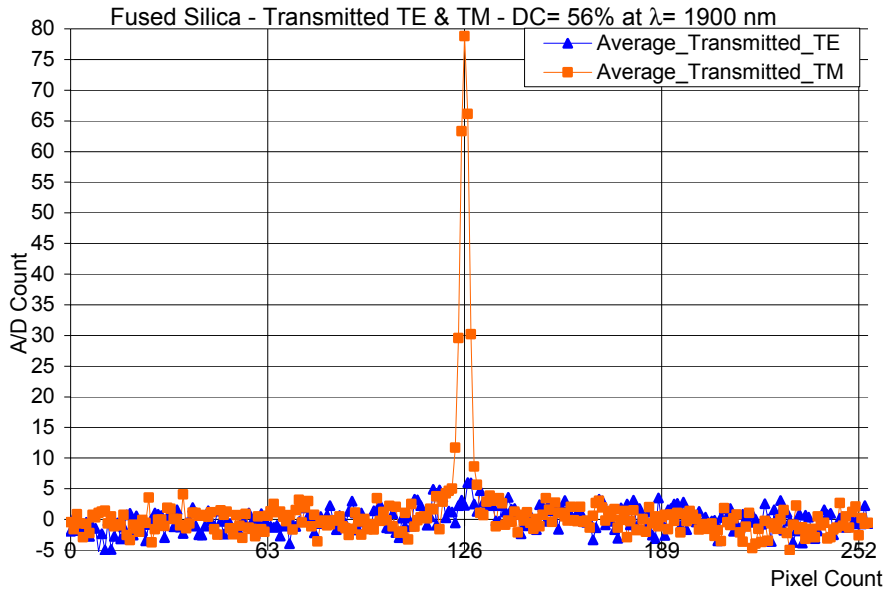

Figure 1.5 Measured TM and TE intensity signal profiles for the 56% duty cycle, indicating an extinction ratio of at least 16:1. The two signals are the average of 20 measurements for each polarization. The averaging reduces the random noise due to the low intensity of the incident beam.

The first fabrication yielded only the 50% and 56% duty cycles and the shape of the gold lines were different from the desired rectangle profiles, see Figure 1.4. Figure 1.5 shows a slice across the x-axis of the measured, polarized transmission on a focal plane array at incident wavelength, λ= 1.9 μm for the TE and TM polarizations for the 56% duty cycle device. The signals are noisy because the incident beam is weak. To mitigate random noise we averaged 20 signals per polarization and obtained an extinction ratio of greater than 16:1.

1.3 Fused Silica Devices - Second Iteration

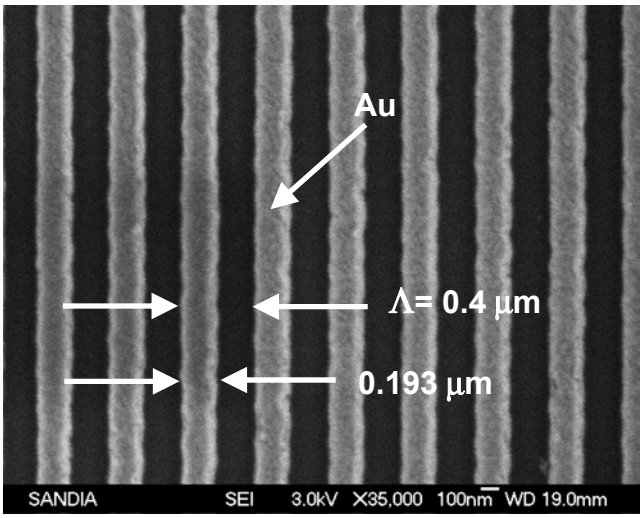

Figure 1.6 SEM of polarizer section with gold lines that have 48% duty cycle. The gold lines are 0.15 μm deep and were placed on a fused silica substrate with a 0.01 μm deep layer of titanium as the adhesive layer.

The e-beam written line width was 0.15 μm with a bias reduction of 25% to produce the desired duty cycle of 50% or line width of 0.2 μm. Several factors affect the amount of bias required such as device size, pattern density and substrate material. Since the performance of the wiregrid polarizer is strongly dependent upon the duty cycle, four devices were fabricated, each one with a different e-beam bias. This approach resulted in devices with duty cycles that varied from 44% to 55%. One of the devices has a measured duty cycle of 48% and its fabrication process is subsequently used for the micro-apertured polarizers. Figure 1.6 shows a SEM of the fabricated devices with a 48% duty cycle.

The devices are tested using a monochromator to select a narrow incident wavelength band from a broad band source. The output polarization of the monochromator initially had an extinction ratio of 3:1, so a polarizer was placed in the beam to improve the source extinction ratio to greater than 1000:1. In addition the characterization process was improved by using a liquid-nitrogen cooled mercury cadmium telluride (HgCdTe) infrared detector and a locking amplifier, facilitating the measurement of the weak TE signal.

The measured extinction ratio, Figure 1.7 (a), is twice what is found in the market while the transmitted TM light is maintain around 80% across the 1.5-3.5 μm spectrum, Figure 1.7 (b). Usually, to increase the extinction ratio the thickness or the duty cycle of the gold wires is increased to the detriment of the transmitted TM polarization. The measured extinction ratio curve is comparable to the curves predicted by the FDTD and RCWA simulations. The measured and simulated curves show a rise in extinction ratio as the wavelength increases. This increase is due to the relative period of the wires compared to the wavelength. For λ= 2 μm the period is Λ= 0.2λ, and for λ= 4 μm the period is Λ= 0.1λ. As the wire grid period decreases the transmitted TE light decreases.

The measured transmitted TM, Figure 1.7, (b) or TE, Figure 1.7 (c), signals follow expected behaviors. While the extinction ratio keeps increasing as function of wavelength, the actual transmitted light decreases rapidly after the wavelength exceeds 3.5 μm. This is expected given that the imaginary coefficient of the refractive index of fused silica is significant at larger wavelengths. This coefficient in a dielectric is related to the absorption of the material.

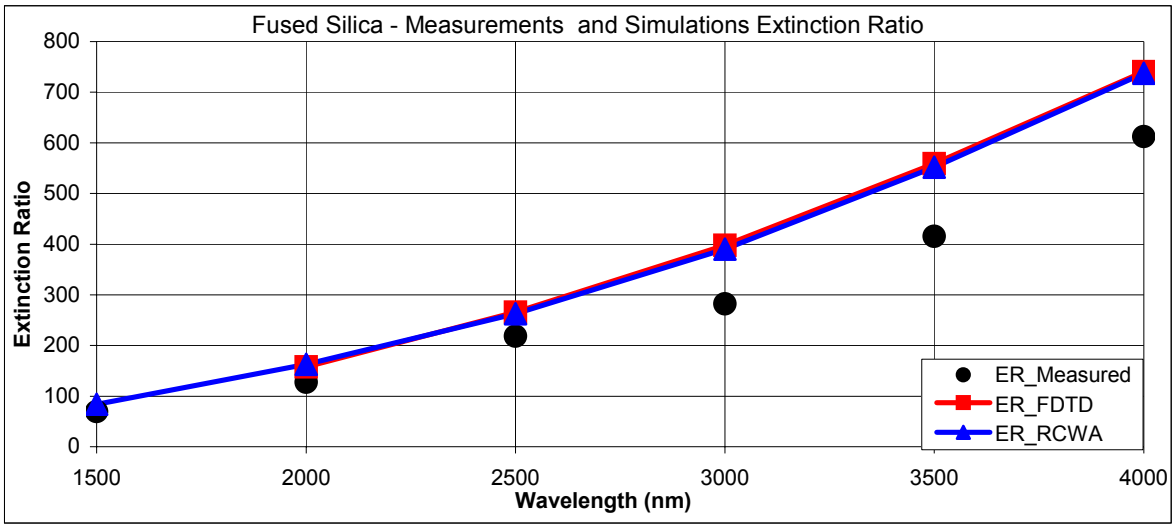

(a)

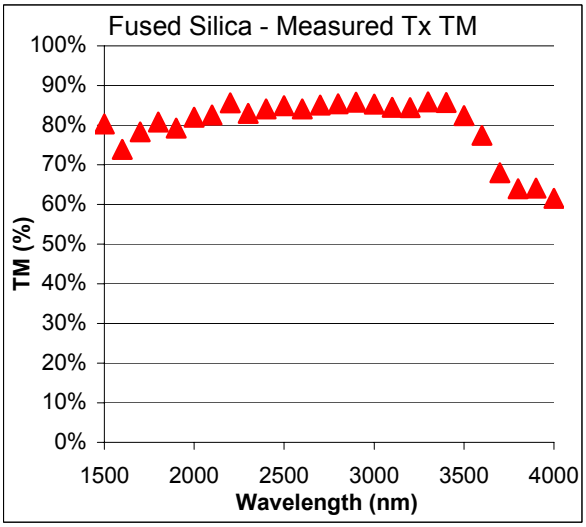

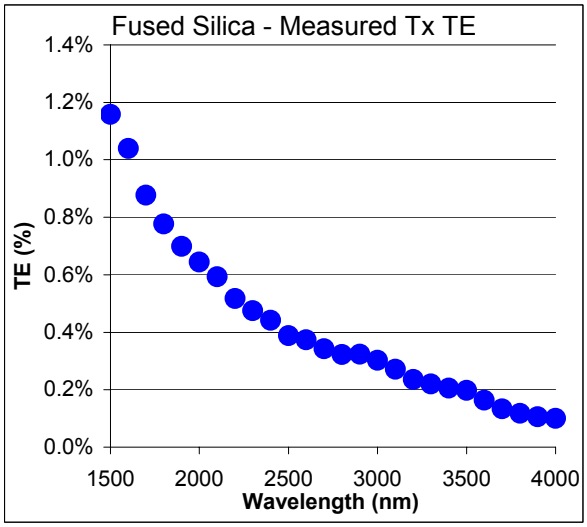

(b) (c)

Figure 1.7 (a) Measured extinction ratio from 1.5 to 4 μm along with simulation results from RCWA and 2D-FDTD[12] periodic boundary simulations. Notice that the extinction ratio exceeds 100:1 through the 2-4 mm spectral range. Measured transmitted (b) TM and (c) TE signal, Figure (b), show consistent behavior with simulations, including the drop in TM and TE signal for wavelengths larger than 3.5 μm

1.4. Focal Plane Array Pixel Size Wiregrid Polarizer

Snap shot imaging polarimetry requires four times the number of pixels to generate an image than a standard camera. A decent image can be reconstructed from 256 x 256 pixels, then a device with 512 x 512 pixels is required for this application. The typical size of a pixel in a high pixel count (> 512 x 512) FPA is between 20 to 25 μm. Furthermore, there are cameras with pixel sizes of 15 by 15 μm. It is expected that devices with even higher pixel counts will be fabricated, with even smaller pixel sizes. Hence, we look at pixel sizes that are smaller than 20 μm, where diffraction and near-field effects are pronounced. Furthermore, some applications will be at longer wavelengths (8 to 12 μm) with even more significant diffraction effects; this is equivalent to having 30 μm pixels at λ= 10 μm, or having a 10.5 μm pixels at λ= 3.5 μm.

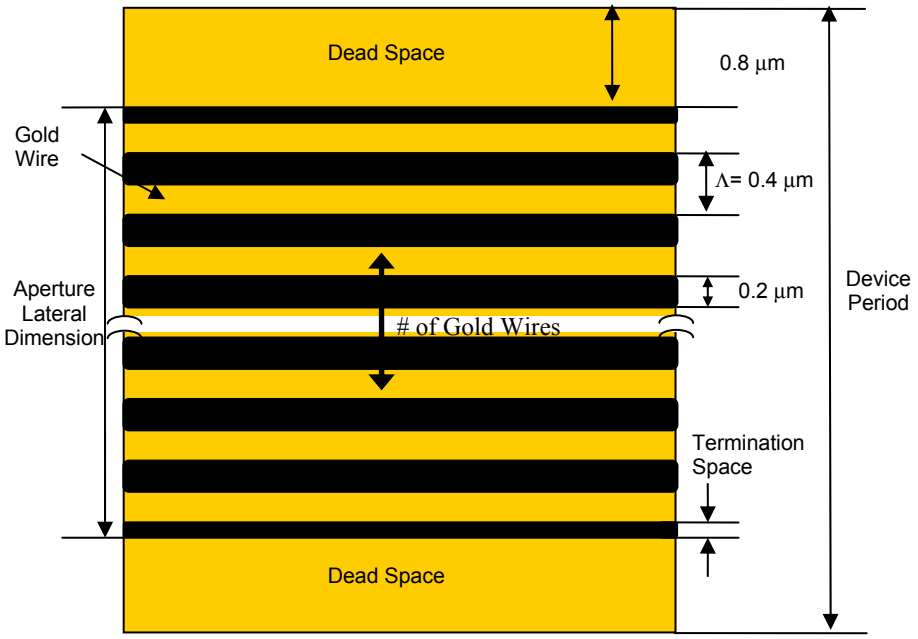

Figure 1.8 The 2D-FDTD model uses a constant period (Λ= 0.4 μm), duty cycle (50%), and depth (0.15 μm) for the gold wires. The model changes the number of lines from 46 (18.4 μm) to 10 (4 μm) plus 0.8 μm of dead space at each end and looks at the effect of varying the termination space for several wavelengths between 2 to 3.5 μm.

We expect that small physical or geometrical variation in any of the wiregrids will affect their performance if the size of the polarizer aperture is comparable to the wavelength. This can be attributed to the wiregrid count, where polarizers with apertures smaller than 20 μm wide have few gold wires (less than 50), while a 10 mm wide device will have 25,000 gold wires. Equally, diffraction effects are pronounced at the micro-polarizer size and they should affect the polarizer transmission efficiency and extinction ratio too. Consequently, it is important to look at symmetry and how the devices are terminated at their apertures.

1.5 Pixel Size Wiregrid Polarizer 2D-FDTD Simulations

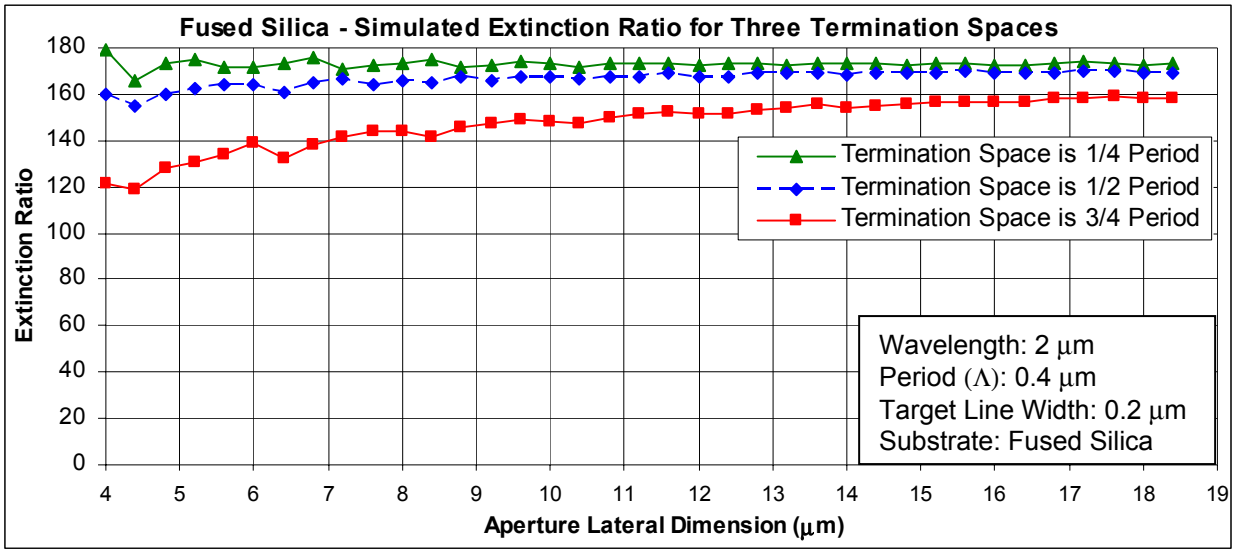

(a)

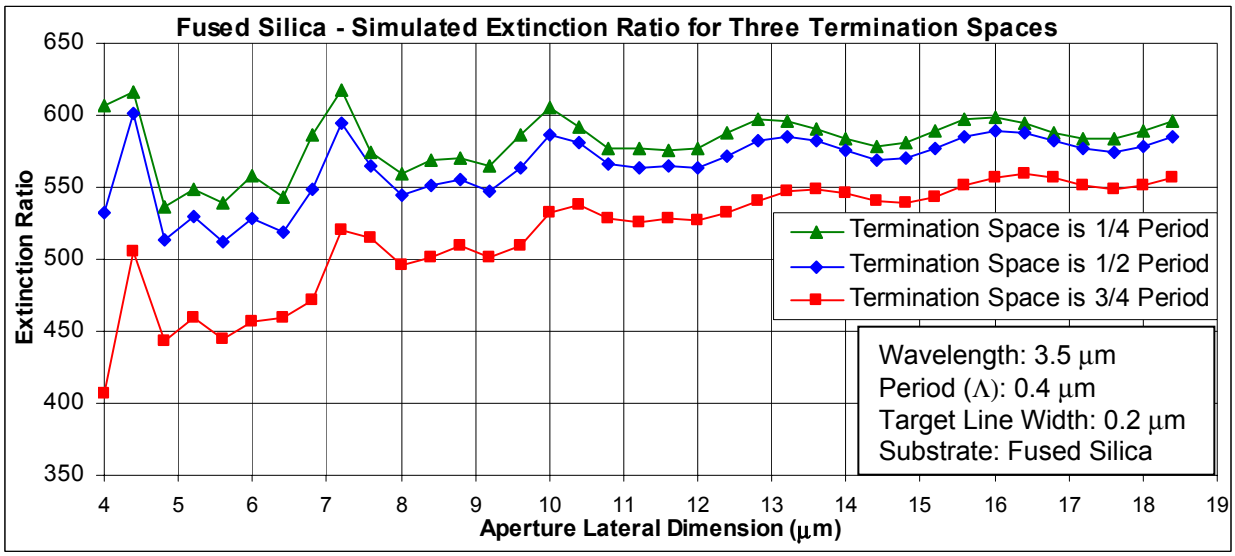

(b)

Figure 1.9 Simulation results show extinction ratio curves from 2D-FDTD model of gold wiregrid polarizers with thickness of 0.15 μm, period (Λ) of 0.4 μm and a duty cycle of 50% at a wavelength of 2 μm, Figure (a) and 3.5 μm Figure (b). The parameters varied are the aperture lateral dimension (the number of lines) and the termination space at the edge. Notice in the curves that as the termination space get smaller the extinction ratio increases.

2D-FDTD code was used to analyze the behavior of the micro polarizer arrays. These elements are small with respect to incident wavelength (2 to 10 waves) and will have pronounced diffraction effects that cannot be analyzed in far field by the RCWA code. The array of micropolarizers is modeled as periodic. This avoids transmission and reflection effects that will corrupt the TM and the TE signals at the perfectly matched layer (PML). The polarizer in the model is made of gold wires, with a rectangular profile of 0.2 μm wide and 0.15 μm thick, on the

surface of a 1.23 μm thick fused silica substrate. The device analyzed can be seen in Figure 1.8. The field is measured 1.3 μm behind the polarizer. All the polarizers have Λ= 0.4 μm gold lines with a duty cycle of 50%. The parameters varied through the simulation are the aperture size, the gold wires count, and the termination edge space at both ends.

Figures 1.9 (a) and (b) show the extinction ratio as a function of the aperture size of the polarizer. Each curve in the Figure represents one of three edge termination spaces: ¼Λ (green curve), ½Λ (blue curve), and ¾Λ (red curve). The difference between the ¼Λ and the ¾Λ termination space is a decrease in extinction ratio of 10%, for the largest aperture, to 33%, for the smallest aperture. This is significant if the application requires a tight control of the extinction ratio across all devices or there is a requirement for larger extinction ratios.

There is an oscillation in the extinction ratio from the middle to the largest aperture in Figures 1.9 (a) and (b). A similar effect is seen in Jensen and Nordin's work[14].

1.6 Pixel Size Wiregrid Polarizers Fabrication

The fabricated devices have wiregrids with a period of Λ=0.4 μm, line widths of 0.2 μm and gold thickness of 0.15 μm with a titanium layer of 0.01 μm. The devices have apertures that range from 18.4 μm to 4 μm. Half of the devices have edge termination spaces of approximately ¼ Λ and the remaining devices have edge spaces of ¾ Λ.

Each micropolarizer is fabricated using the process for the large area polarizers, shown in previous sections. The e-beam writer was biased to write 52% open lines, or 48% duty cycle gold wires. Every micropolarizer is written in the PMMA with an e-beam defined frame that has a width of 2 μm. This frame defines the aperture of each micropolarizer and later facilitates the alignment of a contact mask aperture; see the e-beam delimited frames in Figures 1.10 and 1.12. In addition, the frame makes possible the fabrication of devices that have ¼ Λ and ¾ Λ edge terminations. After depositing the 0.01 μm of titanium and the 0.15 μm of gold the micropolarizers are completed with a lift-off process.

To characterize the devices, the field outside the micropolarizers must be obscured. The obscuration is attained with a gold mask defined by a contact mask and patterned by a liftoff process. The deposited gold has a thickness of 0.2 μm on top of 0.02 μm of titanium. The contact mask has apertures that align to each polarizer written by the e-beam writer. The apertures edge size is 1 μm between the outside and inside perimeters of the e-beam delimited apertures of each polarizer. Figures 1.10 and 1.12 shows the SEM of the e-beam defined aperture around the polarizer and the rounded square of the contact mask. This geometry between the frame and the aperture tolerates a misalignment error of +/- 1 μm between the mask and the e-beam written devices.

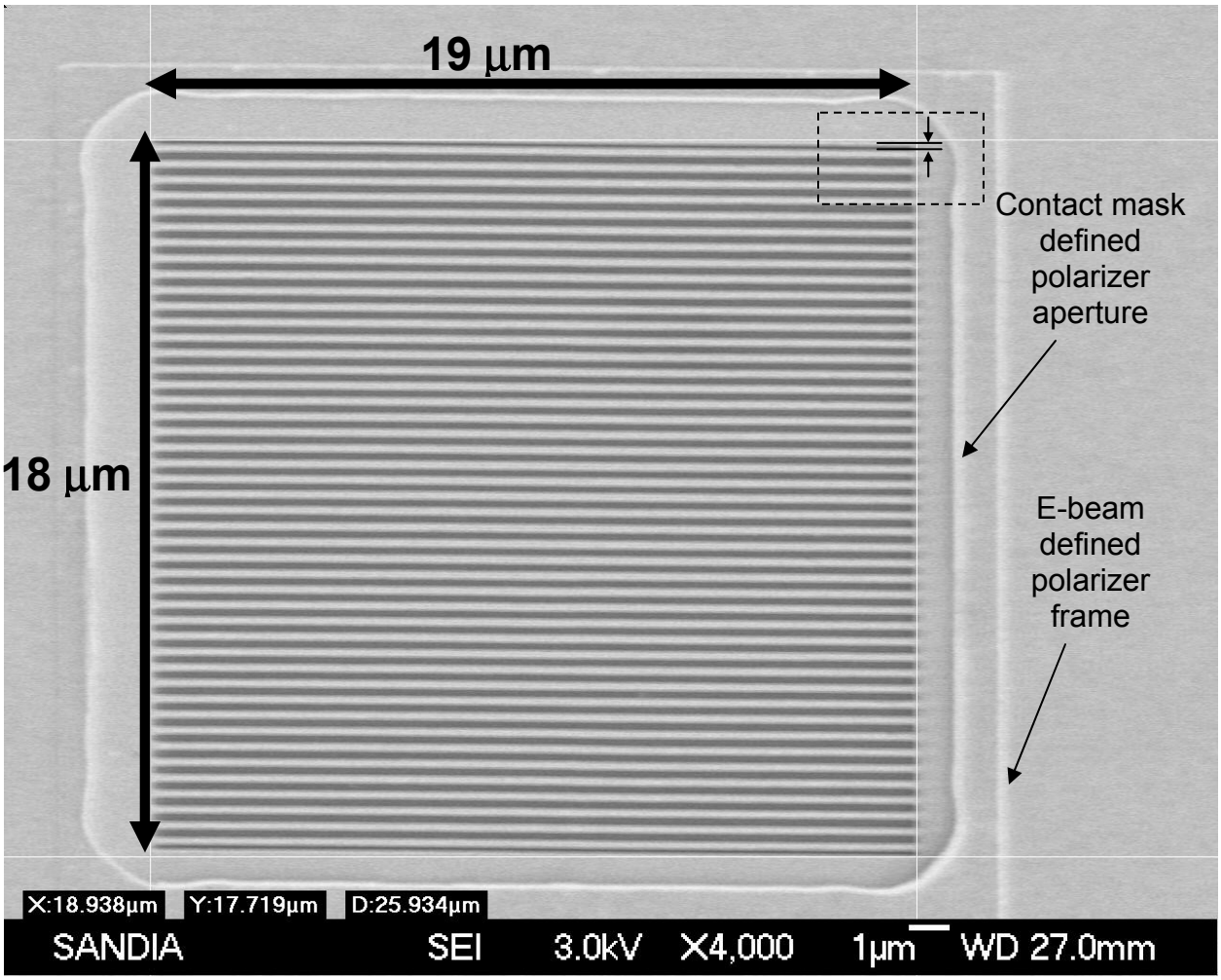

Figure 1.10 SEM image of one of the largest micropolarizer fabricated. The device has 45 gold wires (lateral dimension of 18 μm) of 0.2 μm wide with a period of 0.4 μm and a thickness of 0.15 μm. This device has a termination edge space of about ¼ Λ, see inset.

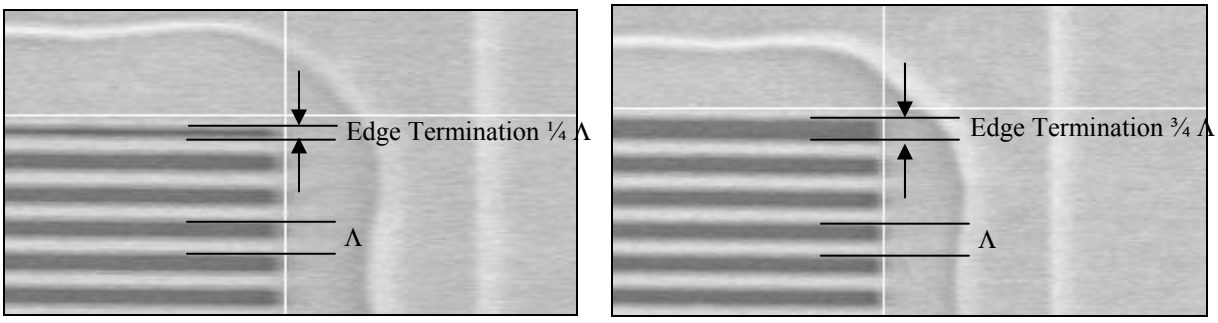

(a) (b)

Figure 1.11 SEM images of the corner showing the edge termination for the two devices with 45 lines but with two different edge termination spaces (a) ¼ Λ and (b) ¾ Λ.

Figure 1.10 shows the SEM of one of the largest devices with 45 gold wires, measuring 19 μm by 18 μm, with a termination edge space of ¼ Λ. Figure 1.11 (a) shows an expanded view of the edge of the same device seen in Figure 1.10. Figure 1.11 (b) shows the expanded view of the edge for an analogous device, but with an edge termination space of ¾ Λ. Figure 1.12 shows one of the smallest devices with 11 gold wires, measuring 4.6 μm by 4.6 μm.

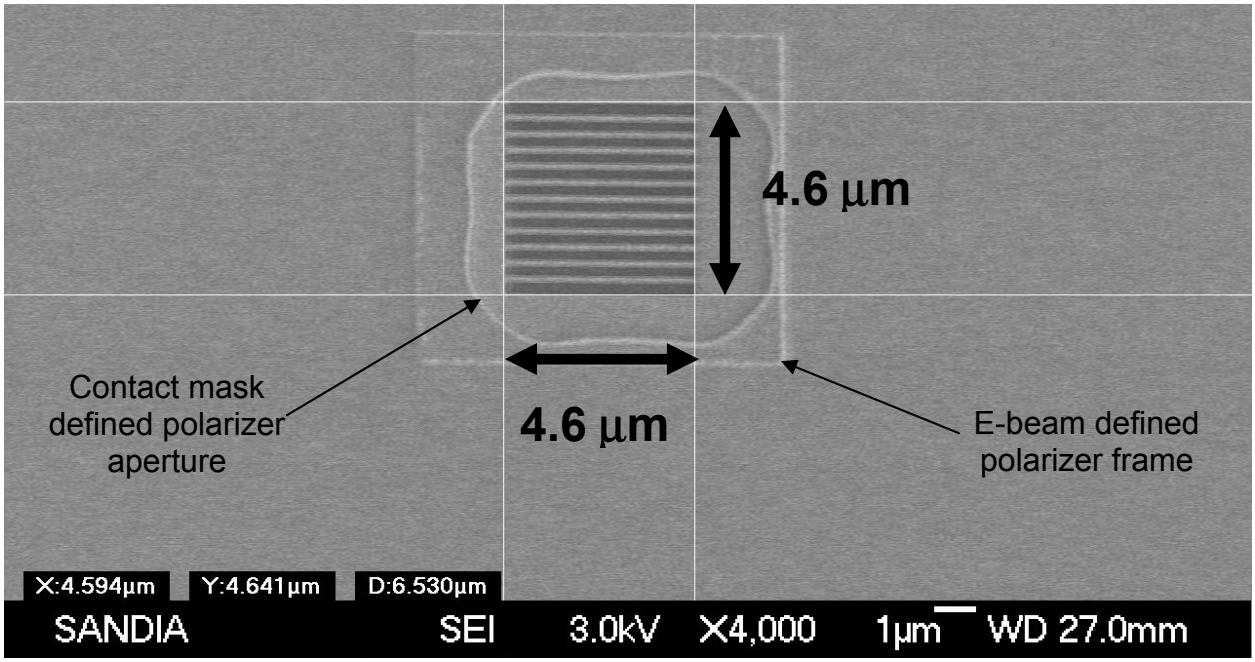

Figure 1.12 SEM image of one of the smallest micropolarizers fabricated. The device (lateral dimension of 4.6 μm) has 11 gold wires of 0.2 μm wide with a period of 0.4 μm and a thickness of 0.15 μm. This device has a termination edge space of about ¾ Λ.

1.7 Pixel Size Wiregrid Polarizers Experimental Results

To test the devices, a linearly polarized 2 mW Helium Neon laser at 3.39 μm is placed in front of the polarizer under test. Subsequently, a fiber-coupled HgCdTe detector is placed in close proximity to the back of the device. The transmitted signal for incident TE and TM linear polarizations is measured for each device and used to calculate the extinction ratio, Transmitted_{TM} / Transmitted_{TE}. The incident TE and TM linear polarizations of the input beam have extinction ratios larger than 1000:1.

The measured extinction ratios as a function of aperture size are shown in Figure 1.13. These data show a similar behavior to those in Figure 1.9 (a) and (b), where the devices have a higher extinction ratio when the edge termination space is smaller, ¼ Λ, than the larger edge termination space of ¾ Λ.

The overall measured extinction ratio, from 200:1 to 50:1; was smaller than simulated with the worst numbers for the smaller aperture devices (compare Figures 1.13, 1.9 (a) and 1.9 (b)). Part of this divergence can be attributed to changes in duty cycle across the fabricated parts. The

larger aperture parts show a gold wire duty cycle of 48%, while the smallest parts show a 40% duty cycle. These deviations in duty cycle between the largest and the smallest devices are attributed to differences in proximity effects when writing the wiregrids with the e-beam writer using the same area dose. Computer models indicate that the 16% to 20% reduction in duty cycle results in a drop in extinction ratio of 64% with respect to a nominal 50% gold wire duty cycle.

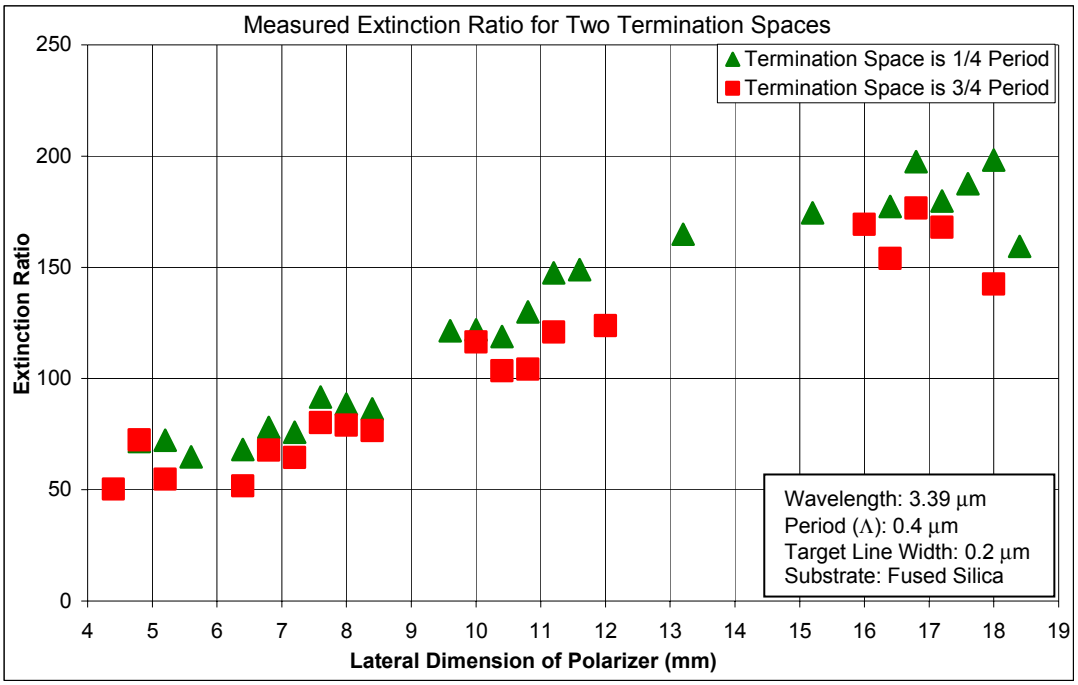

Figure 1.13 Measured extinction ratio data from 74 reduced aperture polarizers. The measured devices ranged in size from 19 µm (46 lines) to 4 µm (10 lines). Notice that the ¼ Λ data has a larger extinction ratio than the corresponding ¾ Λ data. The discontinuity in data is from defective devices.

The characterized transmitted TM signal ranges from 30% for the smallest polarizers to 80% for the largest. The normalized measured transmitted TM signal is presented in Figure 1.14 (a). Figure 1.14 (b) shows the normalized measured TE signal for the same components. The actual transmitted TE and TM signals are larger than the normalized signals since not all light is collected due to diffraction effects and the limited acceptance numerical aperture (NA) of the fiber, 0.22. This effect is most significant for the smallest polarizers.

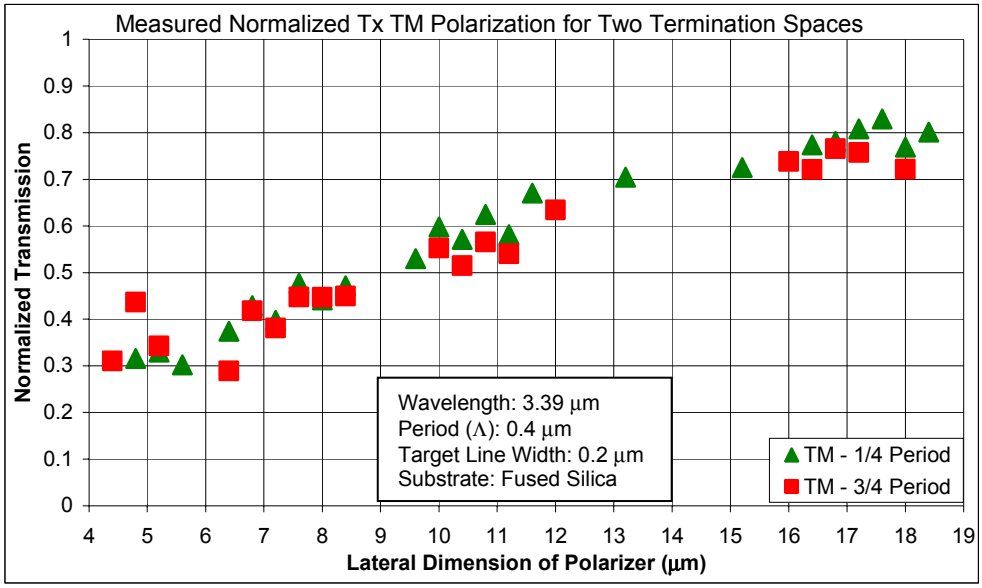

(a)

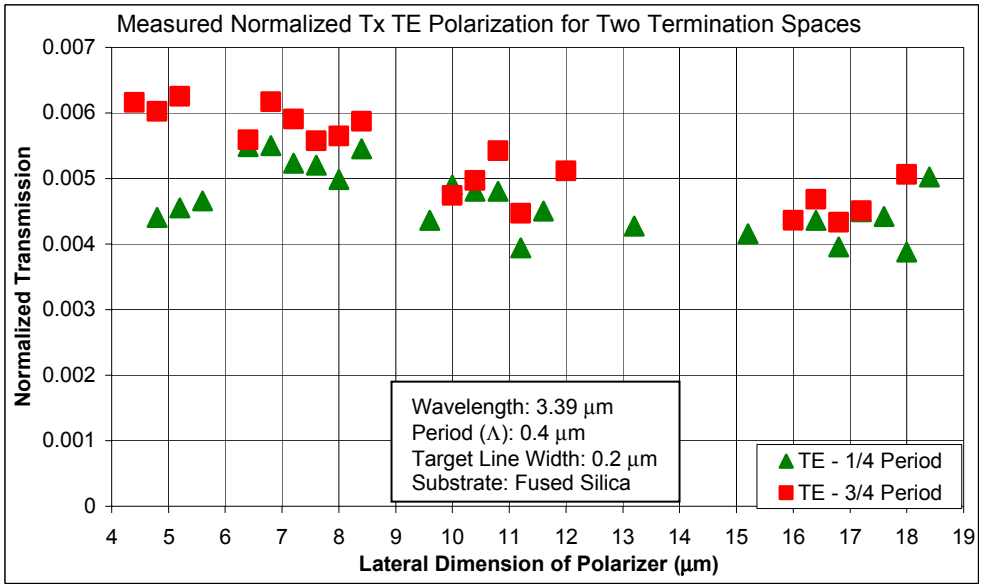

(b)

Figure 1.14 Measured normalized TM (a) and TE (b) data of 74 reduced aperture polarizers. The measured devices ranged in size from 19 μm (46 lines) to 4 μm (10 lines). The measured transmission is smaller than the real transmission due to incomplete collection caused by diffraction effects and the limited acceptance numerical aperture (NA) of the fiber. The discontinuity in data is from defective devices.

1.8 Lithium Fluoride Large Area Polarizers

The fabrication process of wiregrid polarizers in LiF required the use of waterless procedures. Those procedures include eliminating the use of isopropyl alcohol, which contains water and. The substrate should be protected in the backside when using potassium triiodide ($K^+I_3^-$). $K^+I_3^-$ is used as part of the process of writing in PMMA with the e-beam writer.

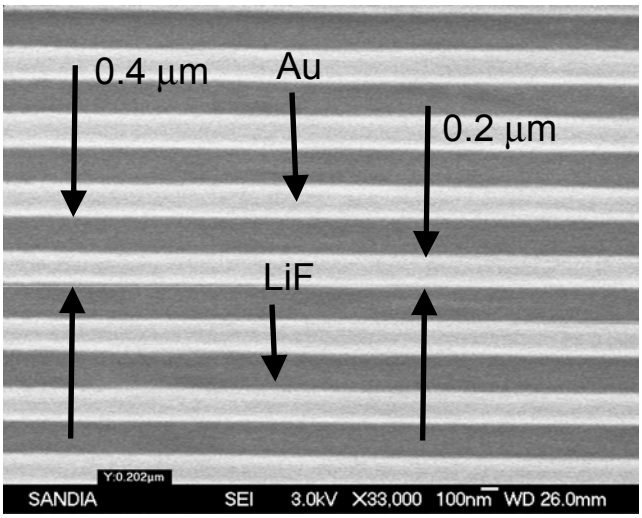

Figure 1.15 SEM of gold wiregrid polarizers on a lithium fluoride substrate. The device has a period of 0.4 µm and a duty cycle of 50.5%, or 0.202 µm wide gold lines. The metal wires are 0.01 mm thick titanium and 0.16 µm gold on top

We have gone through several iterations in the process development of patterning the wiregrids, each time with an improvement in the extinction ratio, see Figure 1.15. However, the desired extinction ratio has not reached the values obtained with the fused silica substrate, see Figure 1.16 (a). Otherwise, the devices transmission of the TM irradiance, Figure 1.16 (b), is mantained at 90% across the MWIR range but the Transmitted TE is not small enough, see Figure 1.16 (c).

Further process development is required that should look at the profile of the wiregrids, the actual thickness of the gold and how it adheres to the LiF substrate. In addition, we should look at possible contaminations and physical degradation inflicted on the substrate during fabrication.

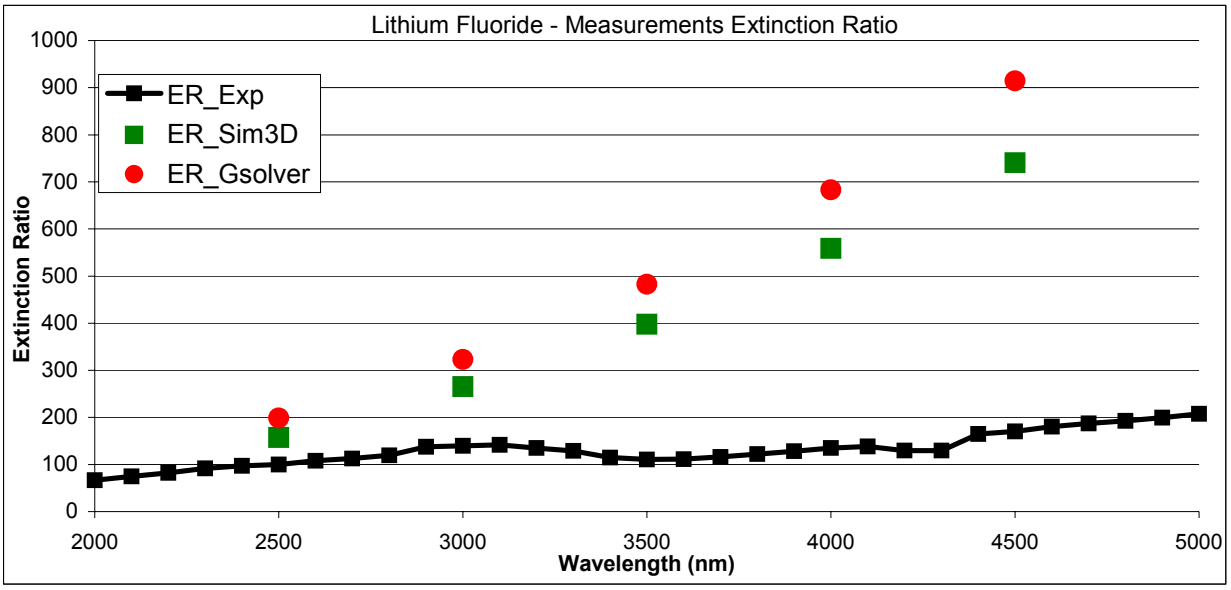

(a)

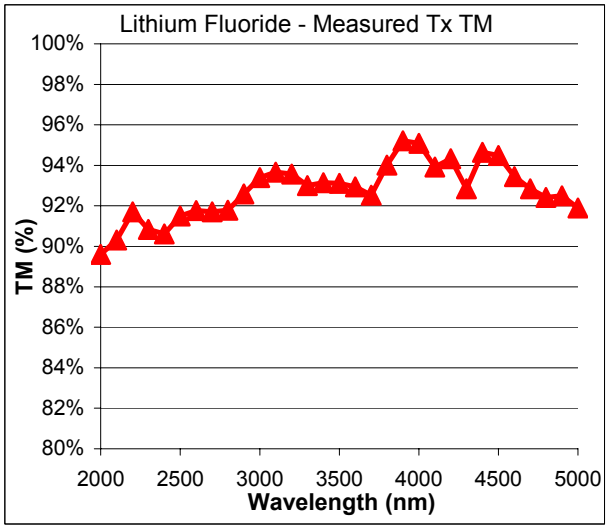

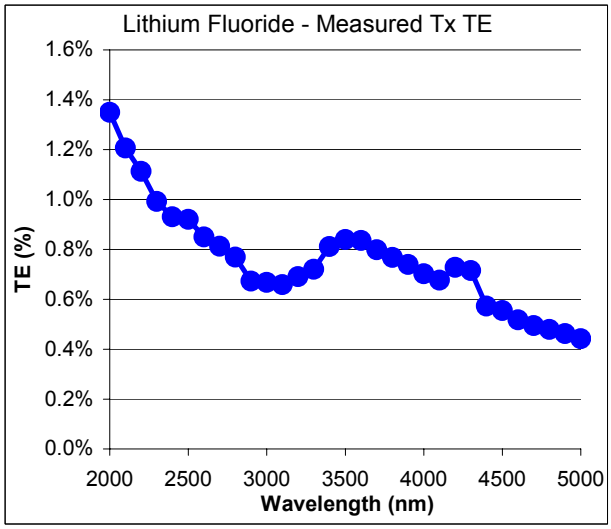

(b) (c)

Figure 1.16 (a) Measurements of the extinction ratio from 2 to 5 µm of gold wiregrid polarizer on a LiF substrate along with simulation results from RCWA and 2D-FDTD[12] periodic boundary simulations. Process development is still required to improve the extinction ratio of the polarizer. The transmitted TM (b) and TE (c) irradiance indicate that LiF can perform across the entire MWIR range.

1.9 Super Pixel Simulations

While there are some simulation data in the literature on the behavior of pixelated polarizer arrays[13, 14], most of these works focus on the behavior of the pixel performance (e.g. extinction ratio and TM transmission) versus wiregrid count, metal density, pixel size, etc. Our interest is in understanding the behavior of the electromagnetic field as it propagates away from the super pixel array. We believe that as the pixel sizes get small, diffraction effects become significant. This calls for a reduced distance between the super-pixel array and the FPA to minimize crosstalk between pixels.

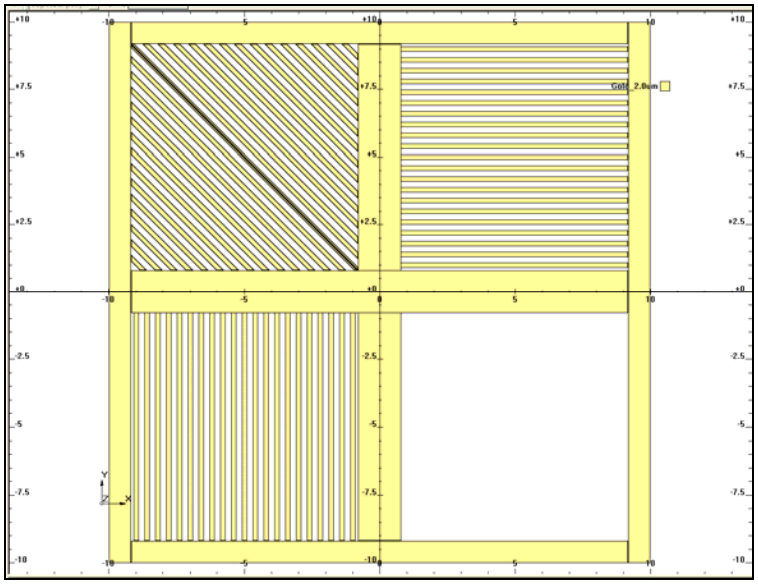

Figure 1.17 FDTD model of a super pixel. The simulation assumes a periodic boundary condition for the x and y axis. PML is defined at both extremes of the z-axis. The simulation propagates a 2 µm plane wave in vacuum to 1.2 µm pass the super-pixel exit plane. The super-pixel has polarizer cells of 8.4 microns wide with 0.2 µm gold lines and a period of 0.4 µm. Each cell is separated by a 1.6 µm wide gold band. This simulation looks at the effect of an open cell and a diagonally oriented polarizer on the extinction ratio of adjacent polarizers.

In addition we want to look at certain combinations of super-pixel geometries. Certain combinations will provide a more direct solution to the four Stokes parameters (Figure 1.17) using this geometry solves Equation 1.1:

$$\begin{aligned} S_0 &= I_T/I_T \quad where \quad I_T \quad is \quad I_{total\ in\ pixel} \\ S_1 &= (2I_1 - I_T)/I_T \quad where \quad I_1 \quad is \quad I(90°,0) \\ S_2 &= (2I_2 - I_T)/I_T \quad where \quad I_2 \quad is \quad I(45°,0) \\ S_3 &= (2I_3 - I_T)/I_T \quad where \quad I_3 \quad is \quad I(45°,\pi/2) \end{aligned} \tag{1.1}$$

I_T is the intensity of the open cell in the super pixel. I_1 is the vertical aligned polarizers, I_2 is the 45° aligned polarizer and I_3 is the output from the horizontal plus a retardance wave plate. The retardance waveplate is not part of these simulations but will be analyzed in later sections. This geometry has an open cell with the highest signals output of the super cell, at least 25% higher than any other cell. This larger signal from the open pixel bleeds into adjacent pixels including the horizontal aligned polarizer, or in TE mode. Intensity profiles from FDTD simulations at a propagation distance of 0.5 µm shown in Figure 1.18 (a), and at 1.0 µm are shown in Figure 1.18 (b). The extinction ratio between the irradiance of the vertical polarizer and the horizontal polarizer for a horizontally polarized input field is 142:1 at 0.5 µm, and 92:1 at 1.0 µm.

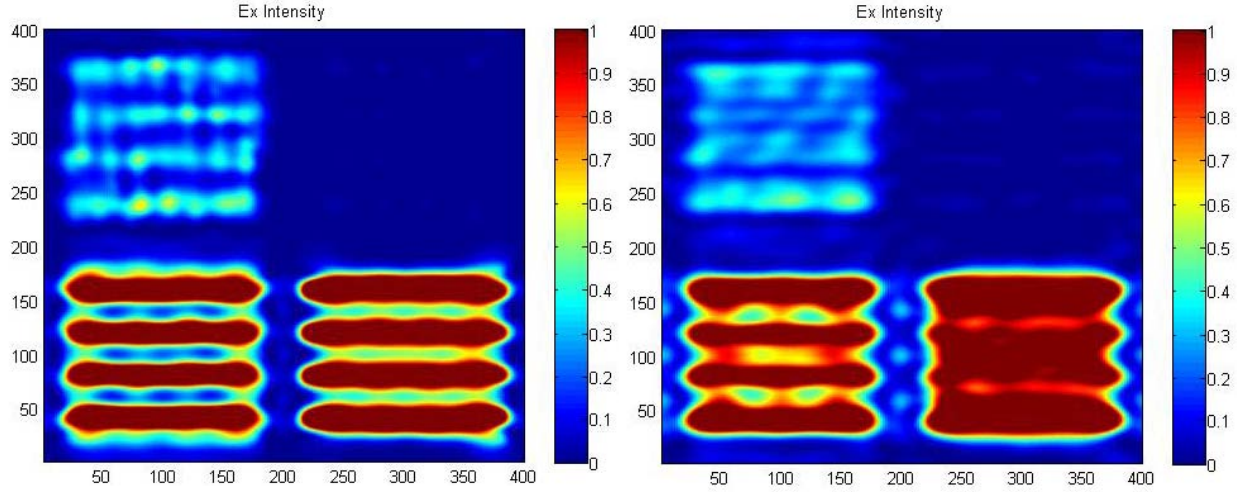

(a) (b)

Figure 1.18 FDTD simulation intensity distributions in the x-y plane at a propagation distance of 0.5 µm (a) and 1.0 µm (b) from the center plane of the super pixel. The extinction ratio between the vertical and the horizontal polarizers is 142:1 at the 0.5 µm plane (a) and 92:1 at the 1.0 µm plane (b). The decrease in the extinction ratio between the two planes is attributed to cross-talk from diffraction by the neighboring diagonal polarizer and the open cell. The open cell is the largest contributor to crosstalk.

The device simulated is depicted in Figure 1.17, and has a cell size of 8.4 µm by 8.4 µm and the overall super pixel size is 20 µm x 20 µm. The device has gold wiregrids with a period of 0.4 µm, a 50% duty cycle, and 0.15 µm thick wiregrids. The simulation uses a periodic boundary condition for the x and y axis. However, the input field has a wavelength of 2.0 µm, which makes the aperture of the polarizer 4.2 waves. An equivalent cell size for a 5 µm input field is 21.0 µm; a pixel size comparable to commercially available FPAs.

We use the output field from the FDTD program and transfer it to a physical beam propagation program. The output irradiances at different distances from the polarizer are shown in Figure 1.19. Notice how the output of the open cell diffracts and expands into the cell with the horizontally aligned polarizer (TE field for this case). The simulation does not assume a periodic boundary. However, in a real case the horizontal polarizer will also be diffracted not only from the bottom cell, but from the cell on top of the next super-pixel. It is worth mentioning that the output in the simulations show intensity bars that are aligned along the direction of the polarization of the input field. This indicates that the output field may have a strong diffractive component perpendicular to the polarization direction.

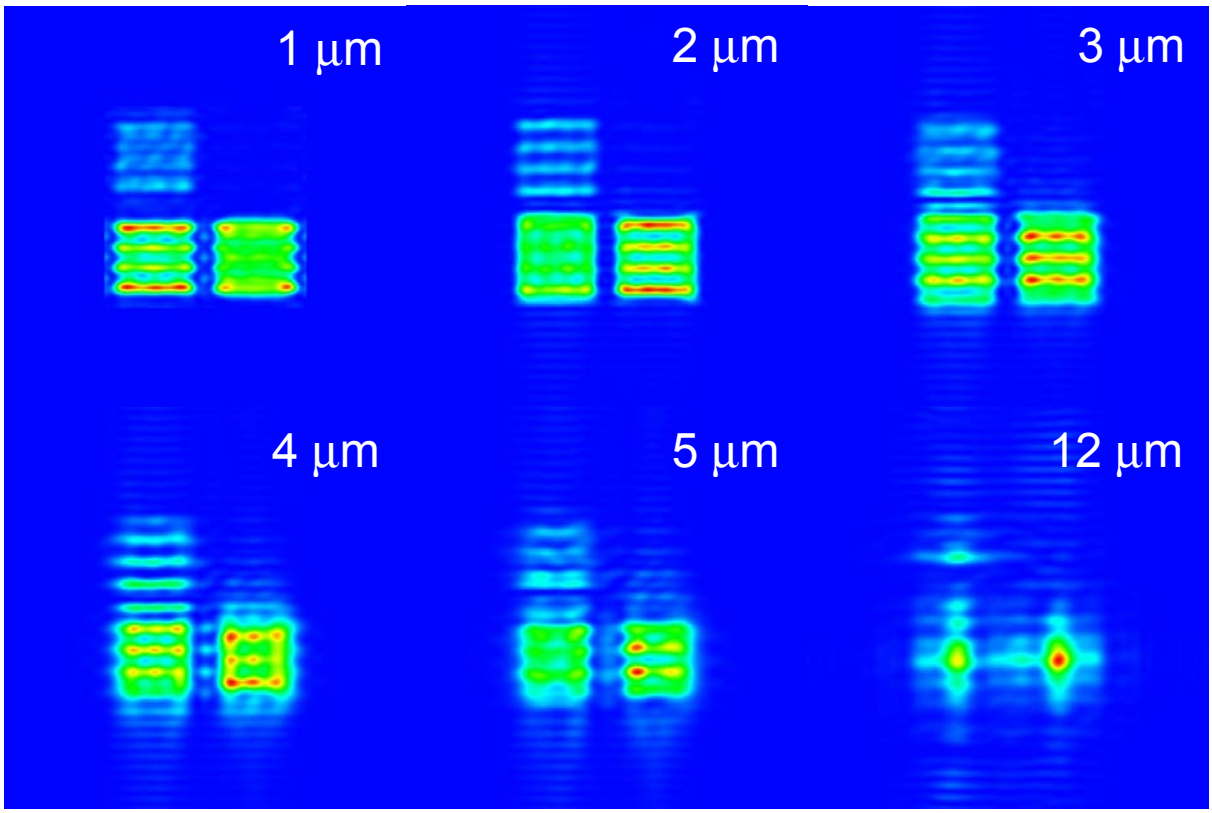

Figure 1.19 Simulation of the propagation of a plane wave, with wavelength λ= 2 µm, after passing through a super-pixel set. The propagation looks at the behavior of the plane wave up to a propagation distance of 12 µm. The starting field for the simulation is obtained from the output field of the FDTD simulation for the super pixel case with an open cell. The super pixel has a period of 20 µm.

A similar simulation is done using the FDTD tool that changes of the geometry of the super-pixel, see Figure 1.20. In this case, a diagonally oriented polarizer replaces the open cell. The orientation of the polarizer is perpendicular from the other polarizer in the top-left corner. This geometry finds the Stokes parameter by solving Equation 1.2:

$$\begin{aligned} S_0 &= I_T/I_T \quad where \quad I_T \quad is \quad \Gamma(I_0 + I_{90}) \\ S_1 &= (2I_1 - I_T)/I_T \quad where \quad I_1 \quad is \quad I(90°,0) \quad or \quad I(0°,0) \\ S_2 &= (2I_2 - I_T)/I_T \quad where \quad I_2 \quad is \quad I(45°,0) \\ S_3 &= (2I_3 - I_T)/I_T \quad where \quad I_3 \quad is \quad I(135°,\pi/2) \end{aligned} \tag{1.2}$$

This approach seems to slow down the decrease in extinction ratio as the field propagates away from the device, see Figure 22. The measured extinction ratio at 0.5 µm is 180:1, Figure 1.21 (a), and 152:1 at 1.0 µm, Figure 1.21 (b). Because $I_T > I_0+I_{90}$, a coefficient Γ should be calculated from measurements done to the polarizers. Γ compensates for attenuation of the vertical and horizontal polarizers at different distances and input polarizations.

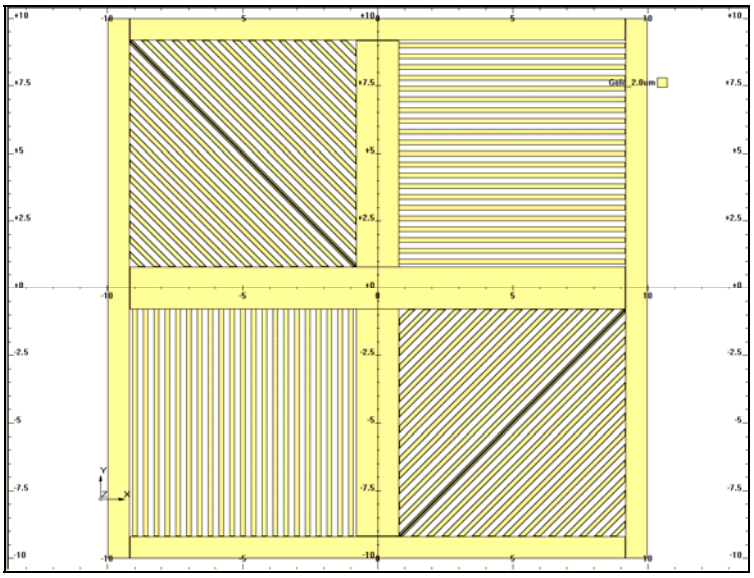

Figure 1.20 FDTD model of a super pixel. The simulation assumes a periodic boundary condition for the x and y axis. PML is defined at both extremes of the z-axis. The simulation propagates a plane wave, with wavelength λ=2 μm, in vacuum to a distance of 1.2 μm past the super-pixel exit plane. The super-pixel has polarizer cells 8.4 microns wide with 0.2 μm gold lines and a period of 0.4 μm. A 1.6 μm wide gold band separates each cell.

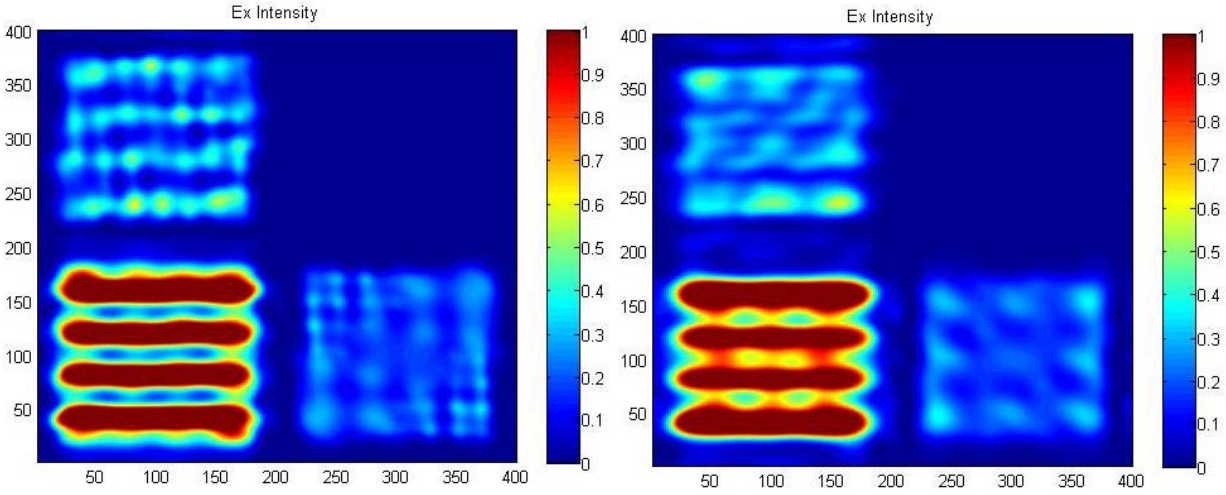

(a) (b)

Figure 1.21 FDTD simulation intensity distributions in the x-y plane at a propagation distance of 0.5 μm (a) and 1.0 μm (b) from the center plane of the super pixel. The extinction ratio between the vertical and the horizontal polarizers is 180.61 at the 0.5 μm plane (a) and 151.83 at the 1.0 μm plane (b). The extinction ratio decreases due to cross talk from diffraction by the diagonally aligned polarizers. However, the decrease is at a smaller rate compared to the super-pixel with the open cell.

Similarly the output of the FDTD simulation is fed to the physical beam propagator and the results of the propagation up to a distance of 12 μm is presented in Figure 1.22, where the most obvious behavior is the reduced signal from the diagonal polarizer into the horizontal polarizer

section. Signal is still bleeding from that cell at the top and bottom of the horizontal polarizer, but it should get an equal amount of cross-talk from the polarizers on the sides.

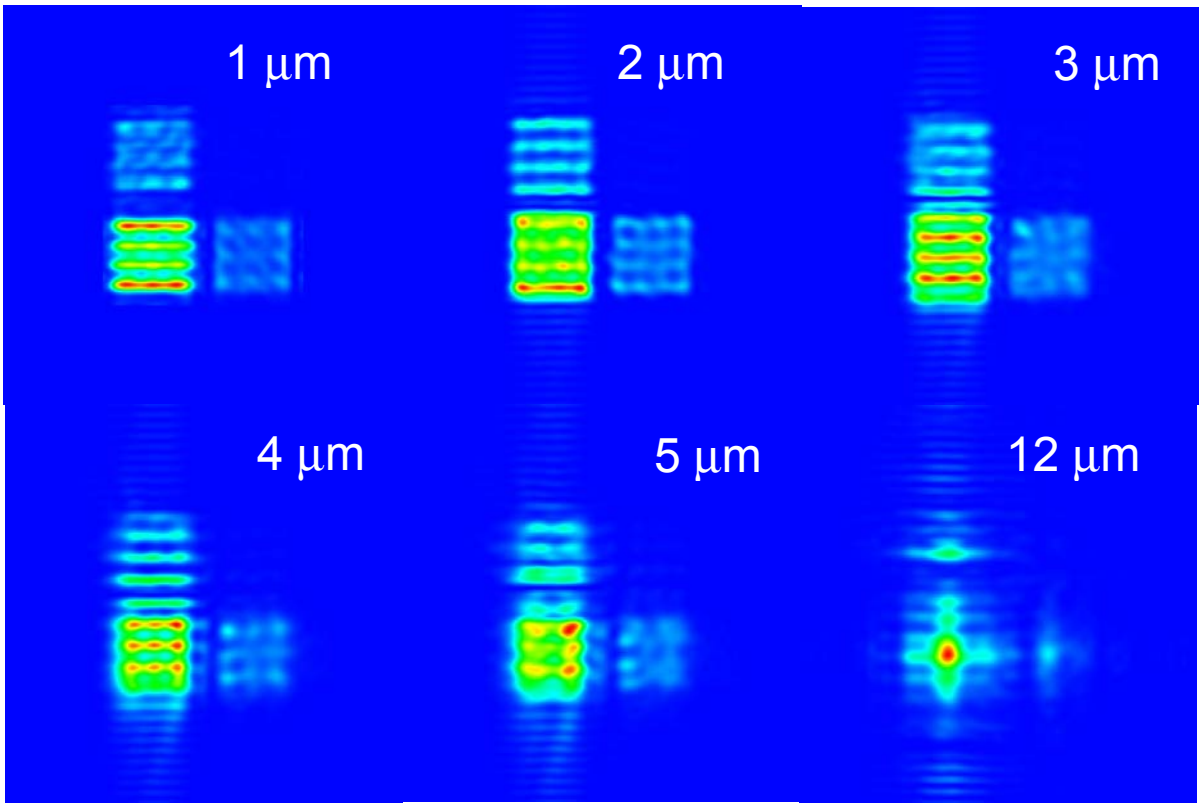

Figure 1.22 Simulation of the propagation of a plane wave, with a wavelength of λ= 2 µm, after passing through a super-pixel set. The propagation looks at the behavior of the plane wave up to a propagation distance of 12 µm. Each image is the propagated beam at a different distance from the polarizer. The starting field for the simulation is obtained from the output field of the FDTD simulation for the super pixel case with no open cells. The super pixel has a period of 20 µm.

Another geometric aspect to consider is the separation between cells. In previous simulations, Figures 1.18 and 1.21, there is a gold frame, 1.6 µm wide, around each polarizer. An alternate possibility is to have no separation between the polarizers, See Figure 1.23. While signal will leak by the proximity to the neighbor cells, diffraction effects will be less pronounced because the relative aperture is larger.

The simulations for this case are done using at a wavelength of 3.39 µm, which is a helium neon (HeNe) line that we also used to characterize devices. FDTD uses a periodic boundary condition for the x-y plane. The polarizer cells are 12.4 µm x 12.4 µm, for a super-pixel size of 24.8 µm in its side; this is about 3.65 waves. The device shows an extinction ratio of 419:1 at 0.5 µm behind the super pixel and 268:1 at 1.0 µm. The polarizers have the same design as in previous simulations, period of 0.4 µm; the wiregrids have a width of 0.2 µm and a thickness of 0.15 µm. The extinction ratio is much larger since the working wavelength is larger, 3.39 µm, for the same polarizer design. However, the extinction ratio drops much faster as the intensity is measured farther away from the polarizer. This is because compared to the wavelength the pixels are

smaller even if they are larger physically. An equivalent polarizer size to the ones analyzed with λ= 2 μm should be about 14.2 μm by 14.2 μm.

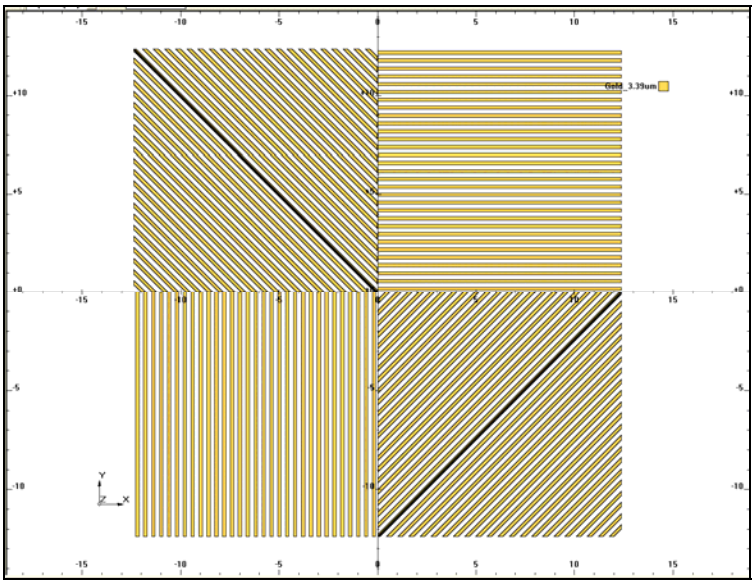

Figure 1.23 FDTD model of a super pixel. The simulation assumes a periodic boundary condition for the x and y axis. PML is defined at both extremes of the z-axis. The simulation propagates a plane wave, with wavelength λ= 3.39 μm, in vacuum to a distance of 1.2 μm past the super-pixel exit plane. The super-pixel has polarizer cells 12.4 microns wide with 0.2 μm gold lines and a period of 0.4 μm. There are no gold bands separating the cells. This simulation looks at the effect of a cell with diagonally oriented polarizers on the extinction ratio of adjacent polarizers.

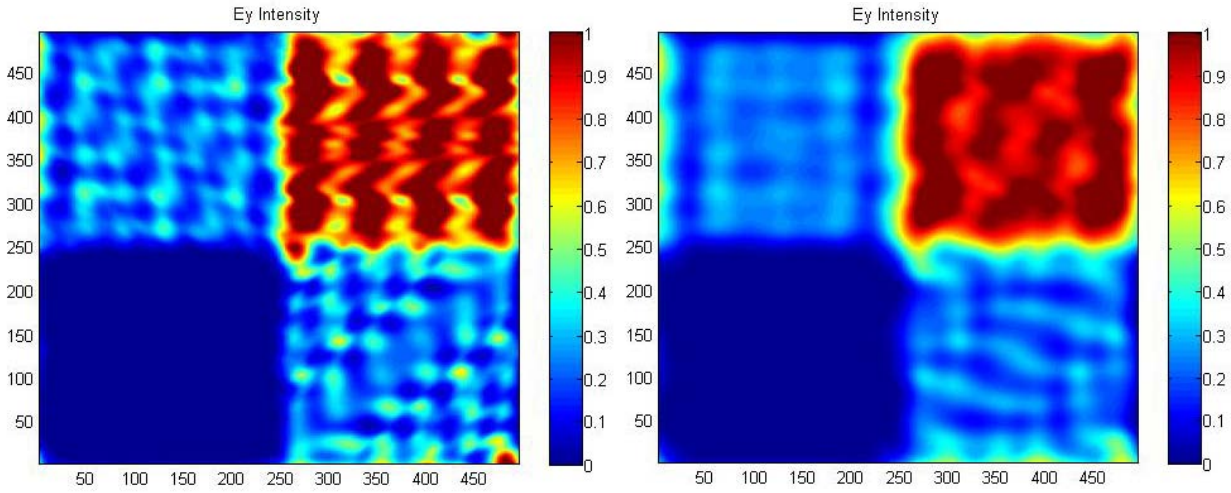

(a) (b)

Figure 1.24 FDTD simulation intensity distributions in the x-y plane at distance of 0.5 μm (a) and 1.0 μm (b) from the super pixel. The extinction ratio between the vertical and the horizontal polarizers is 419:1.at the 0.5 μm plane (a) and 268:1 at the 1.0 μm plane (b). The extinction ratio decreases due to cross talk from diffraction effect by the diagonal aligned polarizers. The extinction ratio is higher for these devices because of the larger wavelength, λ= 3.39 μm, of the input plane wave. However, the relative periodicity of the cells is 3.65 λ, making the super-pixel more sensitive to diffraction effects.

One important aspect of this design are the intensity bands along the axis of the input polarization. See Figure 1.24 for the intensity images at (a) 0.5 μm and (b) 1.0 μm. The output field from the FDTD simulation is fed to the physical propagator and we look at the behavior of the beam at different planes behind the polarizer. The propagation to 20 μm shows cross-talk into the vertically aligned polarizer (bottom-left and TE oriented polarizer) from the diagonal polarizers in the top-left and bottom right corners.

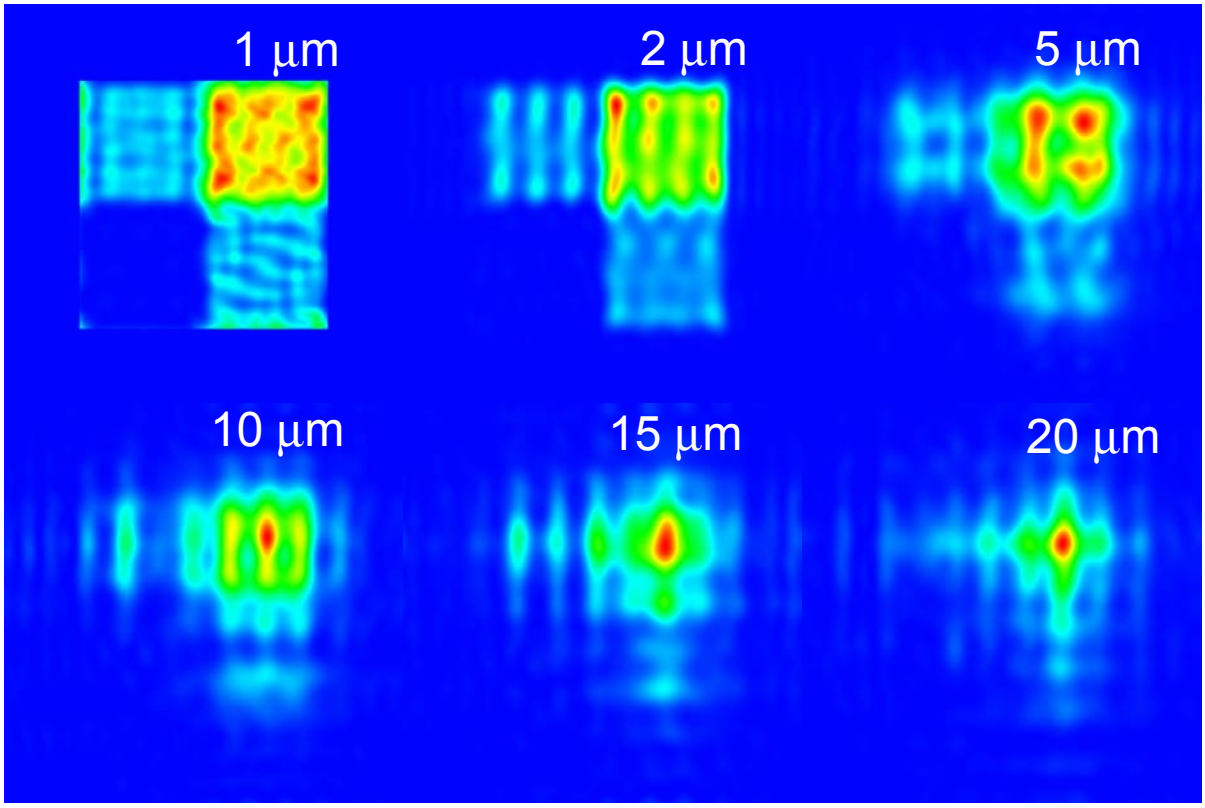

Figure 1.25 Simulation of the propagation of a 3.39 μm plane wave after passing through a super-pixel set. The propagation looks at the behavior of the plane wave up to a propagation distance of 12 μm. Each image is the propagated beam at a different distance from the polarizer. The starting field for the simulation is obtained from the output field of the FDTD simulation for the super pixel case with no open cell. The super pixel has a period of 24.8 μm and no metal separation between the cells.

A third set of simulations help us with a fabricated set of super pixels. These super pixels will have their output imaged in the infrared. Because the pixel size of the FPA on our infrared camera is 30 μm x 30 μm and the pixel count is only 256 x 256 pixels, we decided to fabricate super-pixels with polarizer cell sizes of 30 μm. This is good size to be imaged by our camera system. The devices were tested with a HeNe laser at 3.39 μm; hence, the relative dimension of the pixel is 8.85 waves. This implies that light will diffract at slower rate as it propagates compared to previous simulations.

We want to simulate this new setup and predict some of the behavior of the larger cells. However we are limited by the array size in the FDTD tool. We decided that we can set up an

amplitude mask for an array of pixels with three different attenuations, see Figure 1.26. The equivalent super-pixel array in this simulation has one pixel with 100% transmission, two pixels with 50% transmission and one pixel 0% transmission. The pixel with 100% transmission is equivalent to the TM aligned polarizer, the one with 0% is equivalent to the TE aligned polarizer and the pixels with 50% transmission are equivalent to the diagonally aligned polarizers. However, the results provided by the simulation will only address diffraction effects and will not have polarization differentiation between pixels. The pixels dimensions for this simulation are 30 μm x 30 μm.

A plane wave, with wavelength λ= 3.39 μm, is propagated through this mask and we can see the intensity output at different propagation distances and it behaves similarly than previous propagation simulations. The main difference is that it takes 120 to 150 μm to get similar irradiance profiles. This technique is not reliable to neither get correct extinction ratios nor calculate Stokes parameters but it can give us a reality check on diffraction effects due to the change in pixel size to 30 μm from 15 μm.

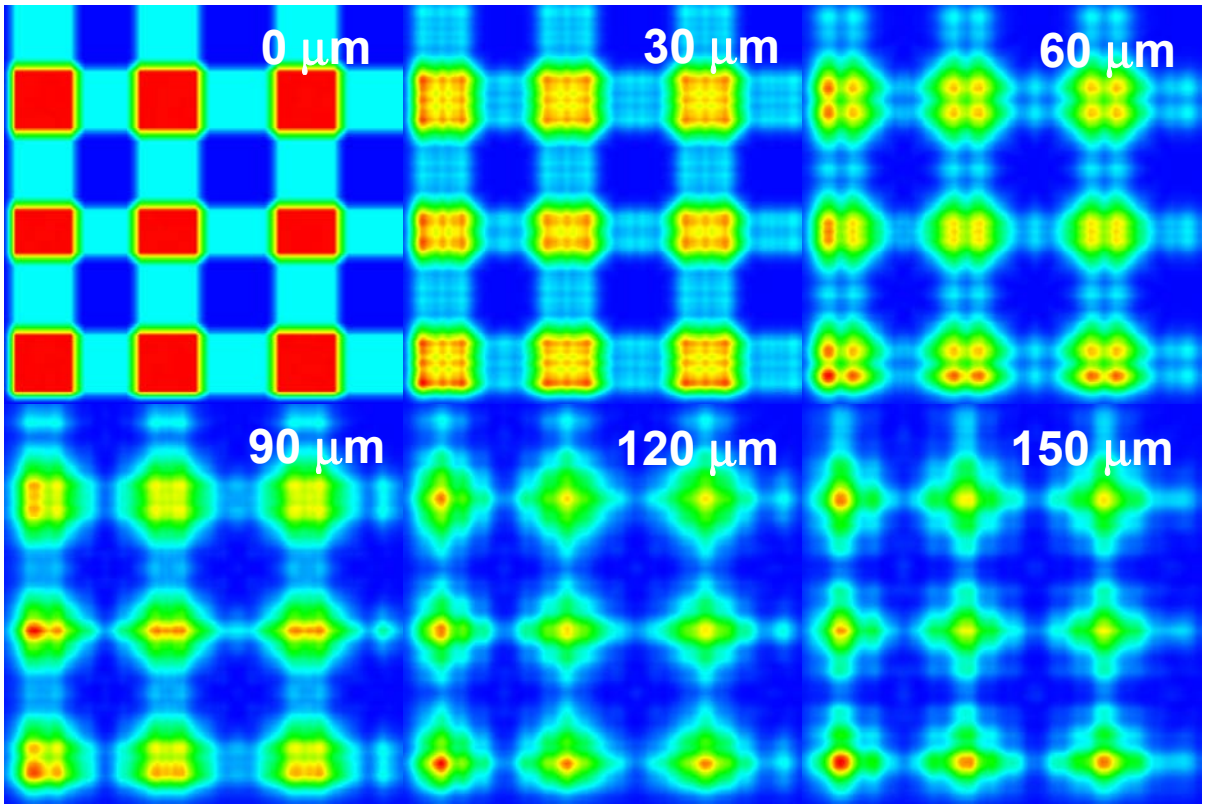

Figure 1.26 Simulation of the propagation of an array of different transmittances that resemble the output of an array of 3 by 3 super pixels. The cell in each super pixel is 30 by 30 mm. The overall dimension of the array is 180 by 180 μm. The simulation does not look at polarization effects but it does consider diffraction effects. Each image is the propagated beam at a different distance from the polarizer.

Distance to Device plane	0 μm	30 μm	60 μm	90 μm	120 μm	150 μm
Extinction Ratio	∞	199.27	60.33	35.51	23.43	17.41

Table 1.1 Calculated extinction ratio at different distances from the simulated device.

Table 1.1 shows the change in extinction ratio for the pixelated amplitude modulation mask at different distances from it. Extinction ratio is the signal in the pixel with high throughput divided by the pixel with minimum throughput. Given that this model is ideal, the signal in the pixel with minimum throughput should be zero and the extinction ratio should approximate to infinity. As the light propagates, the signal in the pixel with minimum signal is not zero and the extinction ratio rapidly degrades.

1.10 Super Pixel Fabrication

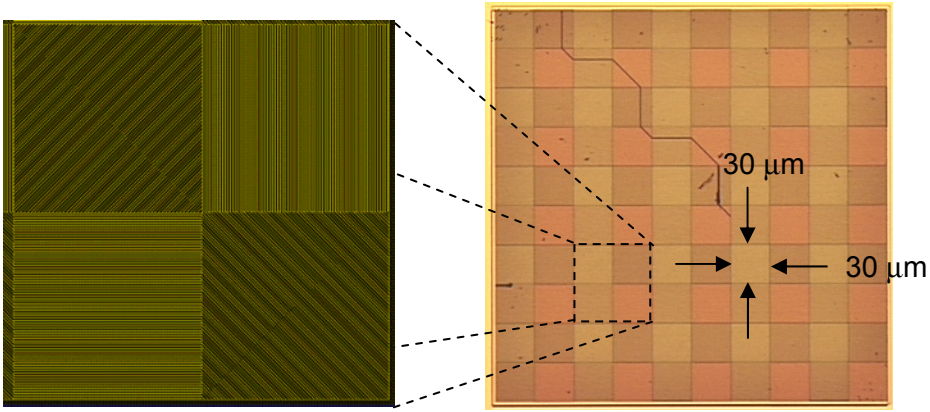

(a) (b)

Figure 1.27 (a) shows layout of super pixel with polarizers oriented (clockwise) 45, 90,135 and 0 degrees, named "No Open Cell #1"; (b) shows a microscope image of a fabricated 5 x 5 array of super pixels with the same alignment of the polarizers as in Figure (b).

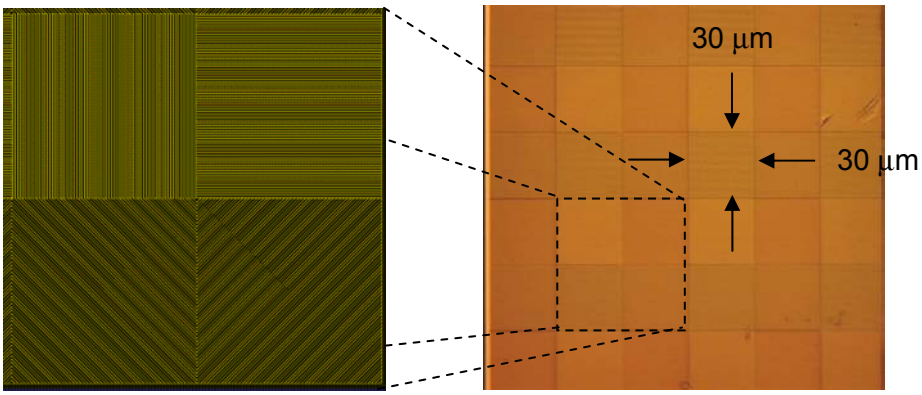

(a) (b)

Figure 1.28 (a) shows layout of super pixel with polarizers oriented (clockwise) 90, 0, 45 and 135 degrees, named "No Open Cell #2"; (b) shows a microscope image of a fabricated 3 x 3 array of super pixels with the same alignment of the polarizers as in Figure (b).

The devices were fabricated in fused silica substrate. This will limit our testing to an spectral range of 2 μm to 3.5 μm; however, it should indicate phenomena seen in our simulations. Because they were tested at a wavelength of λ= 3.39 μm, and each cell size is 30 μm, their relative size is 8.85 waves. For the MWIR range these pixels are large, 15 waves at 2 μm and 6 waves at 5 μm. Typical pixels for this application could be 20 μm, or 10 waves at 2 μm and 4 waves at 5 μm. However, their large size allows us to image them well.

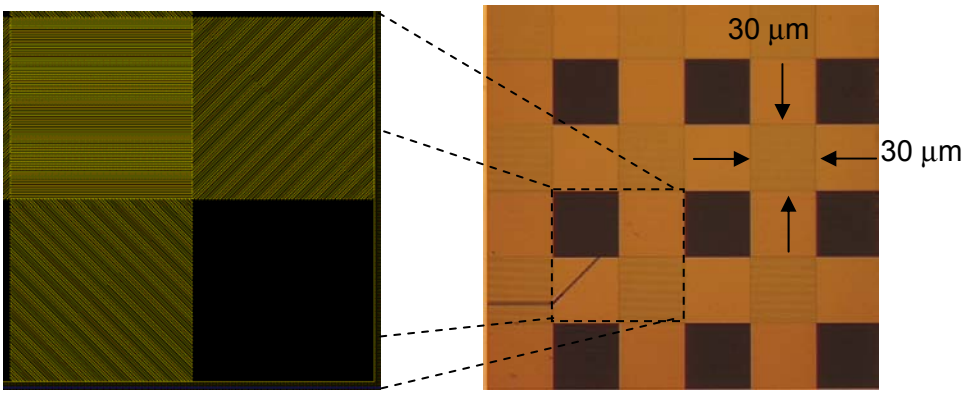

(a) (b)

Figure 1.29 (a) shows layout of super pixel with polarizers oriented (clockwise) 0, 45, open cell and 135 degrees, named "Open Cell #1"; (b) shows a microscope image of a fabricated 3 x 3 array of super pixels with the same alignment of the polarizers as in Figure (b).

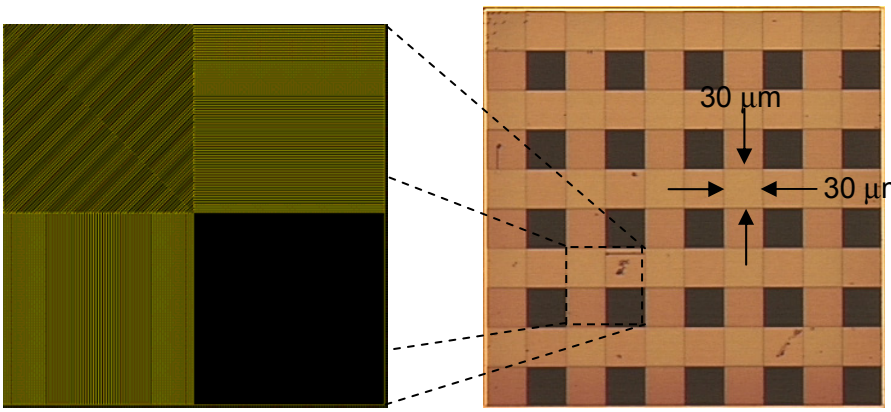

(a) (b)

Figure 1.30 (a) shows layout of super pixel with polarizers oriented (clockwise) 45, 0, open cell and 90 degrees, named "Open Cell #2"; (b) shows a microscope image of a fabricated 5 x 5 array of super pixels with the same alignment of the polarizers as in Figure (b).

Four types of super pixels were made: two with no cell openings and two with cell openings. The first has polarizers aligned 45, 90, 135, and 0 degrees (clockwise from the top left), see layout in Figure 1.27 (a) and named "No Open Cell #1." The second set of devices aligns the polarizers 90, 0, 45 and 135 degrees (clockwise from the top left), see layout in Figure 1.28 (a) and named "No Open Cell #2." The third set of devices aligns the cells 0, 45, Open Cell, and 135 degrees (clockwise from the top left), see layout Figure 1.29 (a) and named "Open Cell #1." The last devices has polarizers aligned 45, 0, Open Cell, and 90 degrees (clockwise from the top left), see layout Figure 1.30 (a) and named "Open Cell #2."

Two array sizes were fabricated for each type of super-pixel: 3 x 3 arrays of super pixels. As in Figures 1.28 (b) and 1.29 (b); and 5 x 5 arrays of super pixels, see Figures 1.27 (b) and 1.30 (b). In addition, four single and isolated pixel cell polarizers were fabricated, see Figure 1.31. Each one aligned 0, 90, 45 and 135 degrees. These four devices can be used to verify single polarizer performance that avoids the cross-talk from adjacent polarizers with different orientations.

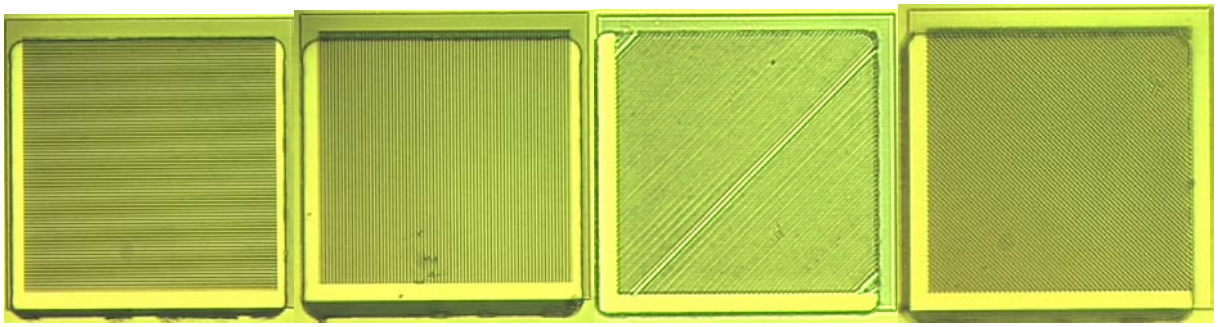

Figure 1.31 Microscope images of 4 fabricated single polarizer cells for the 0, 90, 45 and 135 degree orientation. Each cell measures 30 μm x 30 μm.

The fabricated devices have wiregrids with a period of Λ=0.4 μm, line widths of 0.2 μm and gold thickness of 0.15 μm with a titanium layer thickness of 0.01 μm. These devices were fabricated the same way as previous micropolarizers and large area polarizers.

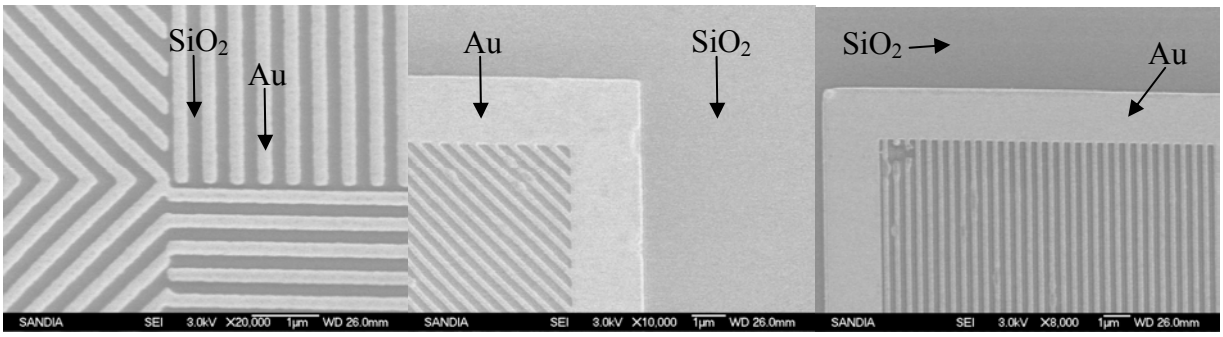

(a) (b) (c)

Figure 1.32 SEM images from different sections of a micropolarizer. Figure (a) shows the center of a super cell, (b) is the corner for a diagonally oriented device and (c) is the corner for a vertically oriented polarizer.

A slight difference is that these devices had the e-beam writer biased to write 48% open lines, or 52% duty cycle gold wires. Every micropolarizer and super-pixel array is written in the PMMA with an e-beam defined frame that has a width of 2 μm. This frame defines the aperture of each device. After depositing the 0.01 μm of titanium and the 0.15 μm of gold the micropolarizers are formed after a lift-off process. The SEM of three sections of a super-pixel array is shown in Figure 1.32. Figure 1.32 (a) is the center of a super pixel "No Open Cell #2." Figures 1.32 (b) and (c) show the corner for diagonal and vertical/horizontal polarizers. The SEM images were taken before applying the contact mask apertures. The contact mask aperture is intended to obscure the outside field of the super-pixel arrays.

1.11 Super Pixel Experimental Results

There is previous work imaging the light coming through micro-polarizer arrays, however, the work is focused on transmission of light through TM aligned polarizers and the extinction ratio[5,6,7,15]. Our work is not only focused on direct performance of the polarizer, but also looks at degradation of the signal coming from the devices. Some of the degradation is related to diffraction effects that create cross talk between pixels.

The devices were imaged with a liquid-nitrogen cooled camera. The camera uses an Indium Antimonide (InSb) FPA that has 256 x 256 pixels; each pixel is 30 µm x 30 µm. Given that the imaging system has a magnification of ~50, each imaged pixel occupies 50 x 50 pixels in the camera. The source used for imaging is a dual line HeNe (1.15 µm and 3.39 µm) with a wavelength selective filter tuned for the 3.39 µm line. The 3.39 µm line has an output of 3 mW and has linear polarization of 500:1. The polarization orientation of the laser is controlled with a Magnesium Fluoride (MgF_2) half-wave plate tuned at 3.39 µm. The half-wave plate allows the rotation of the polarization without having to physically rotate the laser head. The diattenuation at a horizontal polarization is 0.98 and for the vertical polarization is 1.045. Measuring super-pixels has the benefit of no temporal differences among adjacent pixels, when measuring extinction ratio. This is also the advantage of snap shot polarimetry.

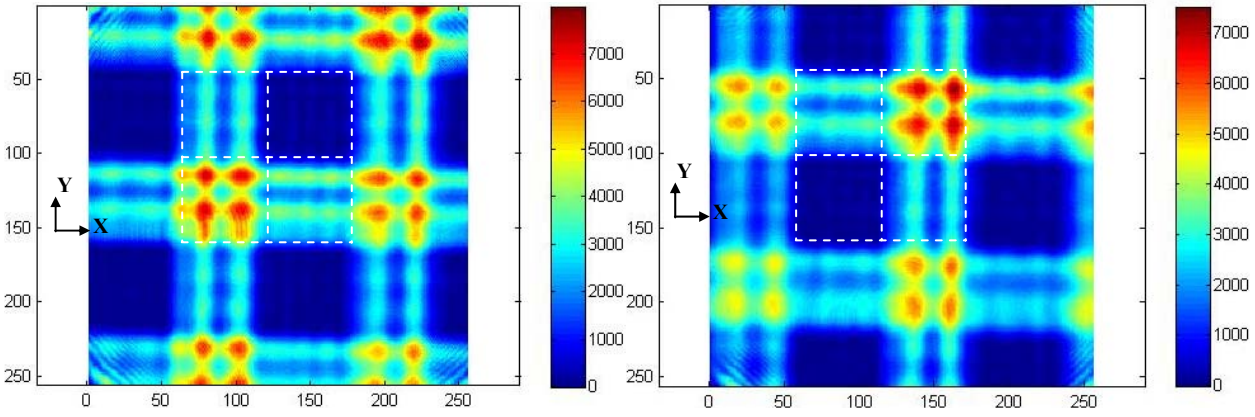

(a) (b)

Figure 1.33 Measured infrared images from a 3 x 3 super cell with polarizers oriented 45, 90,135 and 0 degrees (No Open Cell #1) and an input wavelength of 3.39 µm. Figure (a) has an input polarization aligned to the X-axis and (b) has the polarization aligned along the Y-axis. White dotted lines indicate super-pixel position.

The infrared images (false color) show clearly each polarizer cell for two orthogonal polarizations, see Figure 1.33; one image with input field aligned along the x-axis and the second image along the y-axis. While it is easy to figure out the orientation of a polarizer and its response to a linearly-polarized input field, it is not easy to identify the exact location of the object plane. This is related to internal reflections in the glass from TE, 45 and 135 degree aligned polarizers and the plane of the substrate at the other side of the polarizer. These reflections are coherent and will interfere constructively or destructively at the polarizer plane. Some of that interference is diffracted light from adjacent pixels. This problem could be reduced

by applying an anti-reflection (AR) coating to the substrate on the opposite side of polarizer plane

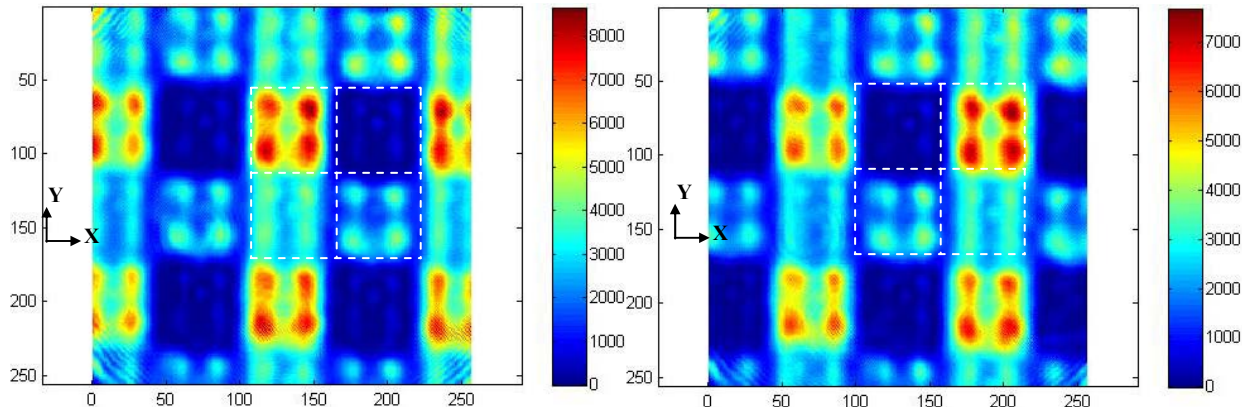

(a) (b)

Figure 1.34 Measured infrared images from a 5 x 5 super cell with polarizers oriented 0, 90, 45 and 135 degrees (No Open Cell #2) and an input wavelength of 3.39 µm. Figure (a) has an input polarization aligned to the X-axis and (b) has the polarization aligned along the Y-axis. White dotted lines indicate super-pixel position.

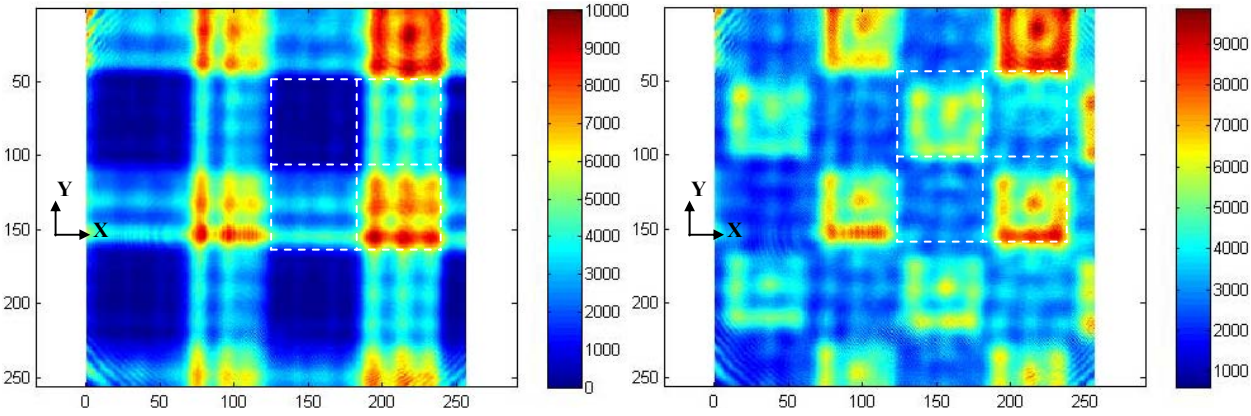

(a) (b)

Figure 1.35 Measured infrared images from a 3 x 3 super cell with polarizers oriented 0, 45, open cell and 135 degrees (Open Cell #1) and an input wavelength of 3.39 µm. Figure (a) has an input polarization aligned to the X-axis and (b) has the polarization aligned along the Y-axis. White dotted lines indicate super-pixel position.

The best device is the "No Open Cell #1," see Figures 1.33 and Table 1.1. This can be attributed to the diagonal location of the two measured polarizers. However, the extinction ratio is only 50:1. The other two devices "No Open Cell #2," see Figures 1.34, and "Open Cell #2," see Figures 1.36, have extinction ratios around 20:1. In the "No Open Cell #2" devices the TE and TM polarizers are aligned in the same axis; while "Open Cell #2" has an open cell aligned to the x and y axis of the two measure polarizers. The "Open Cell #1", see Figures 1.35, did not have its extinction ratio measured given that it has a 45 and 135 aligned polarizers. However, it has an open cell aligned to the x or y axis of the polarizers and it is expected to behave like the "Open Cell #2."

The devices were measured with the metal away from the laser and the metal toward the laser, see Table 1.1. But there is no clear benefit of using one side or the other.

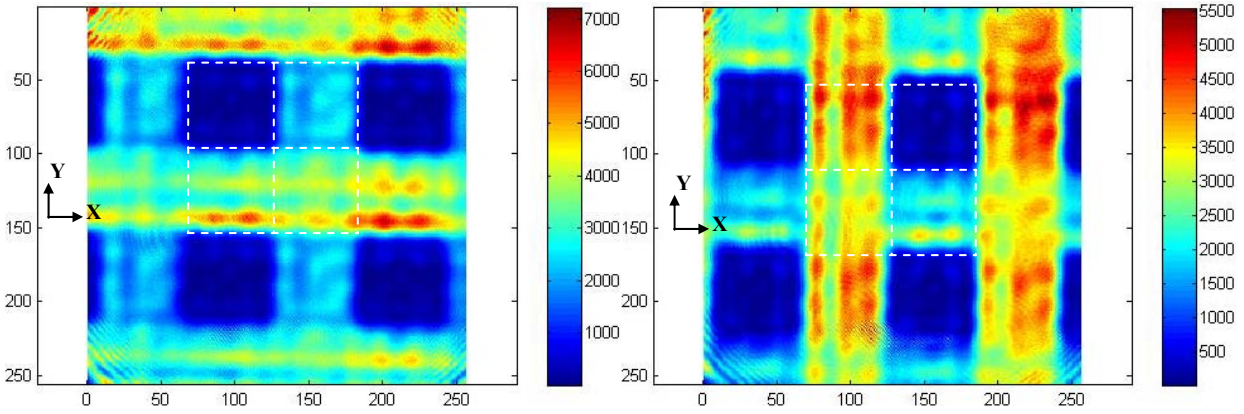

Figure 1.36 Measured infrared images from a 5 x 5 super cell with polarizers oriented 45, 0, open cell and 90 degrees (Open Cell #2) and an input wavelength of 3.39 µm. Figure (a) has an input polarization aligned to the X-axis and (b) has the polarization aligned along the Y-axis. White dotted lines indicate super-pixel position.

The comparison between 5 x 5 super-pixel arrays and 3 x 3 super pixel arrays does not provide a conclusive answer to the amount of light arriving from adjacent pixels, but the results are slightly biased for the 3 x 3 super-pixels with a larger extinction ratio. A 5 x 5 super-pixel arrays has more pixels from where light can diffract into a pixel of interest. Consequently as the number of super pixels decrease the extinction ratio should improve.

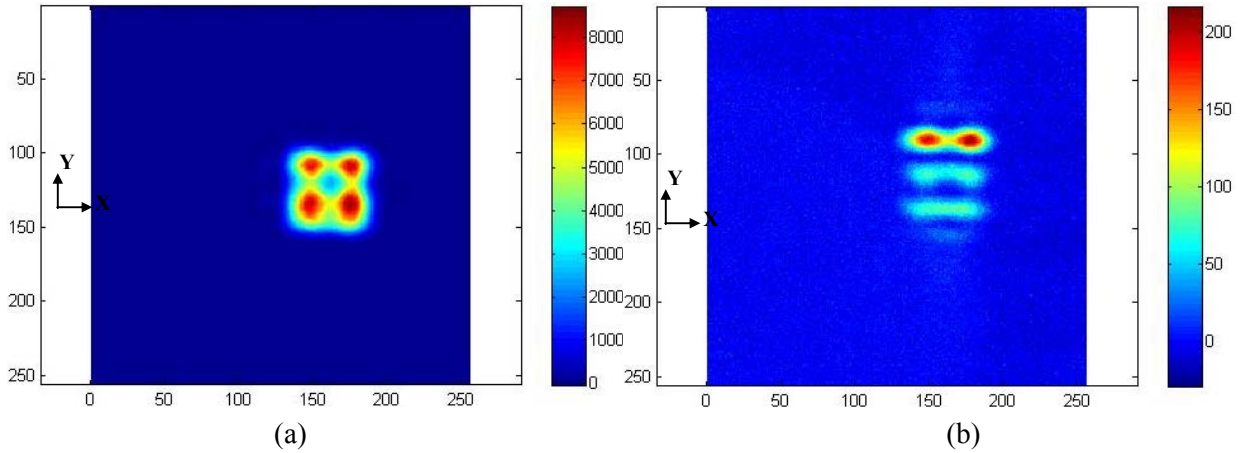

Figure 1.37 Measured infrared images from a vertical aligned polarizer and an input wavelength of 3.39 µm. Figure (a) has an input polarization aligned to the X-axis (TM) and (b) has the polarization aligned along the Y-axis (TE). This polarizer has a unique TE irradiance profile that exceeds the boundaries of the aperture of the polarizer. We are still reviewing this phenomenon.

The best case is when comparing a one cell micro-polarizer with no adjacent devices, See Figures 1.37 and 1.38, for isolated horizontal and vertical polarizers. They have the same dimension as a cell in the super-pixel (30 µm by 30 µm). The horizontal aligned device

measured between 170:1 to 180:1 extinction ratio, see Table 1.2, and the vertical aligned device between: 70:1 to 200:1. The vertically aligned device has an odd intensity distribution in the TE mode that maybe attributed to fabrication anomalies; see Figure 38 (b). These results from single pixels indicate that single polarizers can perform well and cross-talk from adjacent pixels can be an issue when working with super-pixel arrays.

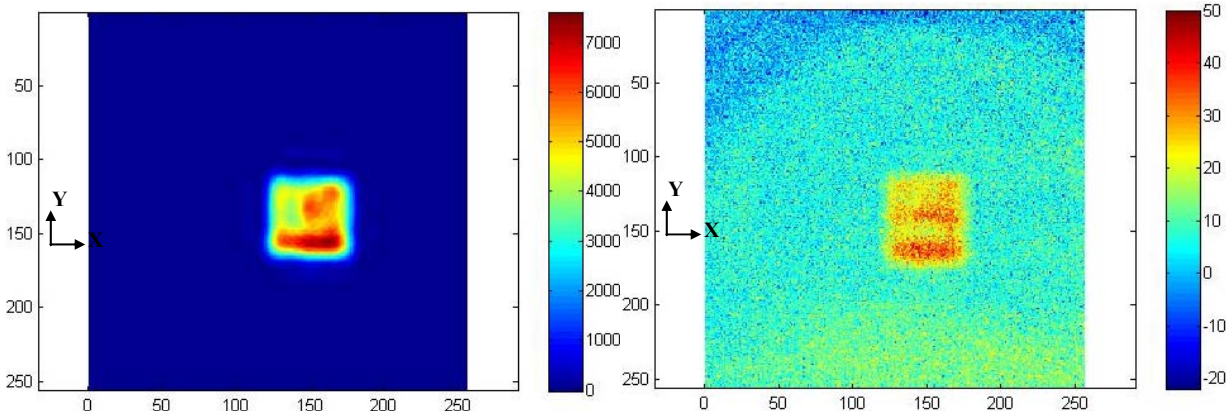

(a) (b)

Figure 1.38 Measured infrared images from a horizontal aligned polarizer and an input wavelength of 3.39 µm. Figure (a) has an input polarization aligned to the Y-axis (TM) and (b) has the polarization aligned along the X-axis (TE).

Metal Away From Laser					Metal Towards Laser				
	No Open Cell #1	No Open Cell #2	Open Cell #1	Open Cell #2		No Open Cell #1	No Open Cell #2	Open Cell #1	Open Cell #2
		3x3					**3x3**		
Ex(⇔)	33.26	20.68	NA	24.64	Ex(⇔)	41.07	15.59	NA	18.72
Ey(⇳)	49.13	26.28	NA	20.98	Ey(⇳)	42.52	19.75	NA	37.24
		5x5					**5x5**		
Ex(⇔)	24.87	26.28	NA	19.72	Ex(⇔)	32.96	24.37	NA	13.15
Ey(⇳)	23.77	27.41	NA	17.88	Ey(⇳)	37.88	29.48	NA	12.09
		1x1					**1x1**		
Vertical Polarizer [1]		158.48 $^{+43.65}/_{-52.88}$			Vertical Polarizer [1]		99.49 $^{+10.74}/_{-25.69}$		
Horizontal Polarizer		178.45			Horizontal Polarizer		174.43		

Table 1.2 Measured extinction ratio for a selected pair of orthogonal micropolarizers, one vertical and one horizontal, per array. There are no results from the "Open Cell#1" type super pixel arrays since they have one cell with horizontally aligned polarizer but it does not contain a vertically aligned polarizer. [1] The single vertical micropolarizer has a range for the extinction ratio given that the TE irradiance extends beyond the perimeter of the aperture of the device. The brackets are different apertures from the standard 30 µm x 30 µm aperture of the micropolarizer.

It is worth mentioning that the infrared signature of a given super-pixel geometry is different from the other super-pixel geometries even if the open areas are the same. This indicates that diffraction patterns are related not only to the geometry defining the single polarizer pixels (square), but also the super-pixel configurations.

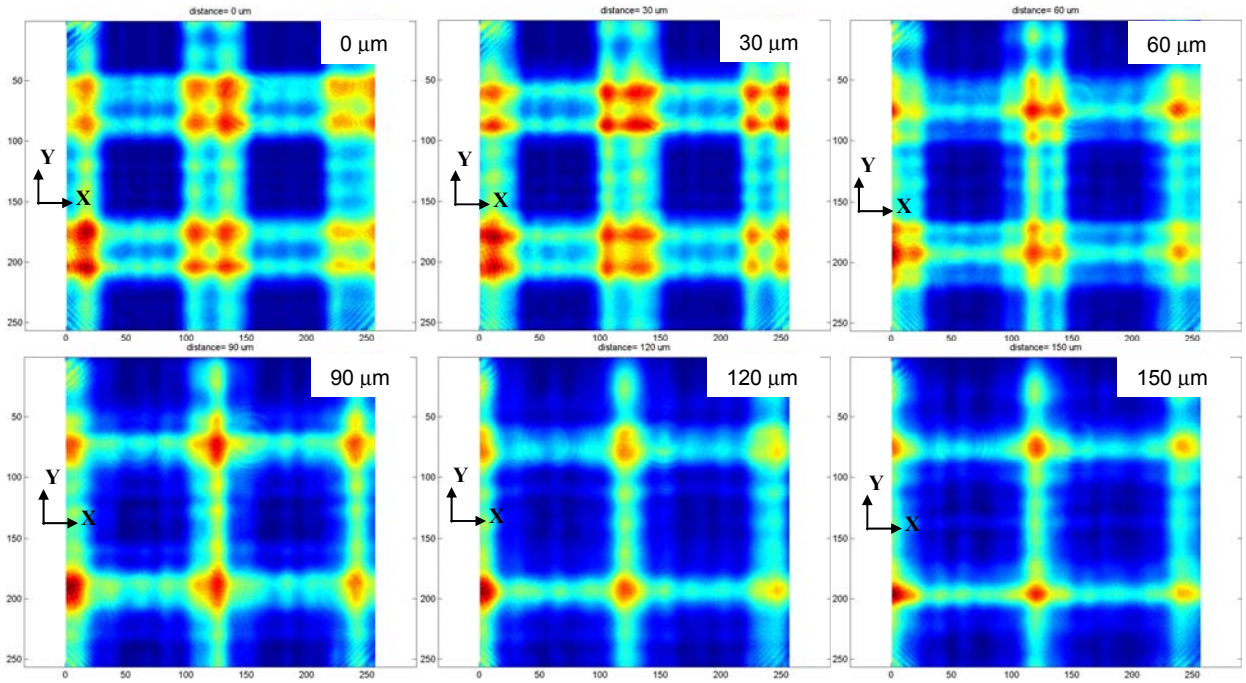

Figure 1.39 Measured infrared images from a 3 x 3 super cell with polarizers oriented 45, 90,135 and 0 degrees and an input wavelength of 3.39 µm polarized along the Y-axis. Each image is the propagated beam at the indicated distance from the polarizer

Figure 1.26 shows the measured propagation of a pixelated intensity distribution. There is no polarization differentiation between pixels but they have an attenuation factor similar to the one seen in the devices fabricated. The pixels in this simulation are 30 µm pixels in their side and are propagated 150 µm with steps of 30 µm.

We took infrared images at different planes away from the 3 x 3 "No Open Cell #1" super pixel array. The images show that the intensities behave similarly, see Figure 1.39 and 1.40 to that on Figure 1.26. Figure 1.39 is the intensity for an input field with polarization aligned to the Y-axis, and Figure 1.40 is the intensity for an input field with polarization aligned to the X-axis.

The differences to the images in Figure 1.26 are related to the signal reflections from the other surface of the super-pixel substrate and the polarization changes induced by each pixelated polarizer. However, the measurement and simulation show a pronounced cross-talk 90 µm away from the micro-polarizer plane for both cases.

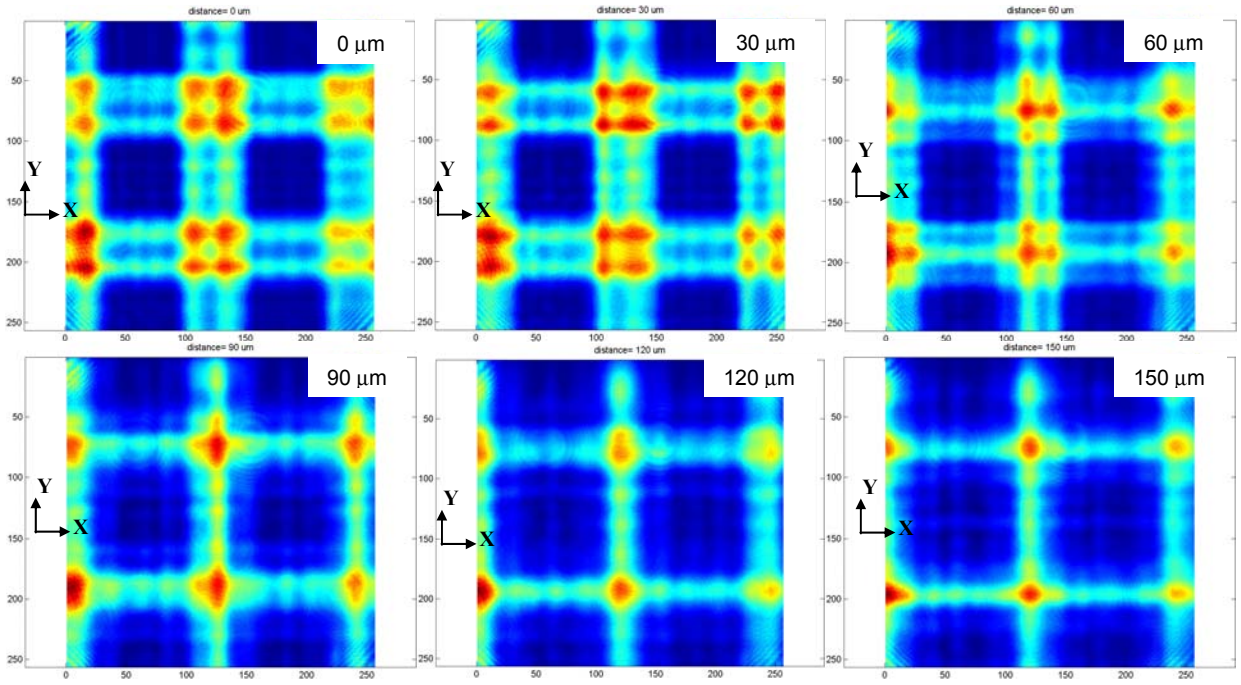

Figure 1.40 Measured infrared images from a 3 x 3 super cell with polarizers oriented 45, 90,135 and 0 degrees and an input wavelength of 3.39 µm an the input polarization along the X-axis. Each image is the propagated beam at a different distance from the polarizer

A measurement of the actual extinction ratio indicates a pronounced drop at 60 µm from the plane of the polarizer, see Table 1.3. The table shows a low extinction ratio at z= 0 µm, or the super-pixel plane, that is not likely due to internal reflections in the fused silica for the TE, 45, and 135 degree aligned polarizers. These reflections include diffraction effects from the small apertures of the reflecting pixels and explain the grid nature of the noise.

Distance to Polarizer plane	0 µm	30 µm	60 µm	90 µm	120 µm	150 µm
Extinction Ratio for Y Polarized Light	21.66	19.62	12.82	8.30	6.64	6.38
Extinction Ratio for X Polarized Light	21.74	16.81	11.35	8.45	7.33	7.32

Table 1.3 Measured extinction ratio for x and y aligned input polarization at different distances from the polarizer. The extinction ratio is low due to etalon effects between the two surfaces of the substrate holding the super-pixel array.

1.12 Conclusions

Large-area gold wiregrid polarizers were designed, modeled and fabricated on fused silica substrates. Extinction ratios greater than 100:1 were measured for wavelengths of 2 to 3.5 µm. The design of these polarizers was used in the modeling and the fabrication of devices that have apertures of 20 to 4 µm. Two set of devices were fabricated, one with a termination edge space

of ¼ Λ and a second set of designs that have termination edge spaces of ¾ Λ. These devices had measured extinction ratios range from 50:1 for the smallest polarizer to 200:1 for the largest one. Compared to previously published results by other groups, these micro-polarizers show an improvement in extinction ratio of 7 to 8 times for devices with apertures of 15 X 15 μm. Simulations predict and measurements confirm that the extinction ratio is larger for the smaller termination edge spacing. In addition, these results indicate the sensitivity of these devices to small and localized deviations from the desired geometry. The results obtained were restricted to 2 to 3.5 μm given that fused silica becomes extremely absorptive beyond the 3.5 μm.

Wire grid polarizers in lithium fluoride substrate were fabricated with the same large area apertures as the fused silica devices. We measured extinction ratios of 60:1 for λ= 2 μm and 200:1 for λ= 5 μm. These devices maintained transmissions equal to or larger than 90% for the whole MWIR range. However the measured extinction ratio is lower than expected. We continue to develop the process to better fabricate these devices.

We quantified near-field and diffractive effects of the finite pixel apertures in transmission. We have designed and built an experimental setup that models a pixel within a focal plane array (FPA) to measure crosstalk from adjacent gold wiregrid micropolarizers. This configuration simulates a snapshot polarization imaging device where the two substrates are stacked; micropolarizer array substrate on top of an FPA. Modeling and measured data indicate crosstalk between the adjacent pixels even after a few microns behind the polarizer plane. Crosstalk between adjacent pixels increases uncertainty in the measured polarization states in a scene of interest. Simulated data confirm that the extinction ratio of a micropolarizer pixel in a small super-pixel, 25 μm x 25 μm at λ= 3.39 μm, will be reduced by 30% when moving the FPA from only 0.5 microns to 1.0 microns away from the polarizer. Experimental data shows that the extinction ratio for an equivalent micropolarizer pixel in a larger super-pixel, 60 μm x 60 μm at λ= 3.39 μm, will be reduced by 32% to 50% when moving the FPA 30 microns away from the polarizer. These changes in extinction ratio are significant for small super-pixels since typical glue separation, usually on the order of 10 microns. Larger super-pixels should tolerate larger separation between super-pixel and FPA, but that will require a corresponding large FPA.

2. Wideband Achromatic Waveplate

2.1 Introduction

Imaging polarimetry provides spatially dependent polarization information from an imaged scene. This data is proving to be extremely useful in many applications. A simplified approach uses a rotating waveplate followed by a fixed polarizer with several sequential images taken to characterize the Stokes parameters across a scene. An alternative to this time sequential approach is a snapshot where the image is divided spatially and the Stokes parameters are determined in parallel. Typical approaches use patterned wire grid polarizers to determine three of the four Stokes parameters with S3, the preference for circular polarization, being neglected. A complete imaging polarimeter would have the capability to determine all four Stokes parameters[3,4,17].

The key element in a complete polarimeter is a quarter-wave plate designed to match the spatial division of the image. Traditional crystal-based waveplates do not easily lend themselves to this type of integration, but elements based on form birefringent gratings can be selectively patterned on a substrate and matched to the desired output pattern. Subwavelength gratings lead to an effective index that is dependent on the incident polarization[10]. This effect is known as form birefringence and can be utilized to provide a waveplate. This paper examines the design of a quarter-wave plate for operation over the mid-IR spectral region, 2 – 5 μm.

The wide spectral band places a stringent constraint on the chromatic variation of the waveplate's phase retardance. Work on achromatic form birefringent waveplates has produced several promising results[18-22]. Subwavelength gratings have been shown to provide a birefringent dispersion that is amenable to providing an achromatic phase retardance[18]; however, previous work has not attempted to cover a spectral band as wide as the one being considered here.

The next section will describe the design approach used to determine the nominal grating design. Section 2.3 will review the fabrication process and Section 2.4 will discuss the experimental results and analysis. Finally, the effect of finite apertures will be considered and areas for future investigation will be presented.

2.2 Design Approach

The quarter-wave plate required for an integrated polarimeter must have individual pixels that match the size of the detector array elements. Using a patterned subwavelength grating leads to form birefringence, which provides the desired phase retardance as well as dispersion that aids the design of an achromatic element[18,21]. The design approach used effective medium theory (EMT)[23-25] to provide a first order approximation that was then optimized using rigorous coupled wave analysis (RCWA)[26,27]. Effective medium theory models a subwavelength grating as a thin film with an effective index determined by the grating materials and incident polarization, see Figure 2.1.

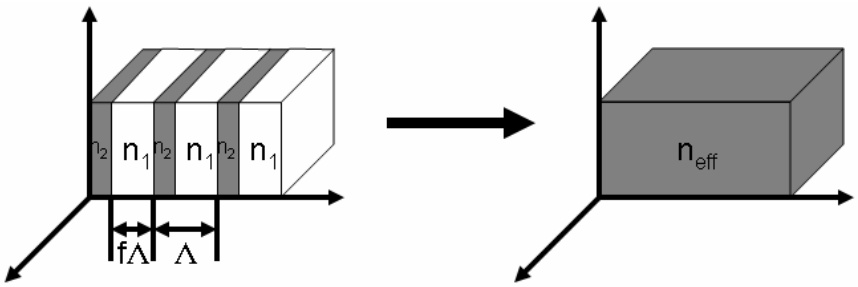

Figure 2.1 Approximation of surface relief grating as a thin film with an effective index dependent on incident polarization.

The effective index for gratings with periods much less than the wavelength are shown in Equation 2.1[10].

$$n_{TE}^{(0)} = \sqrt{f n_1^2 + (1-f) n_2^2}$$
$$n_{TM}^{(0)} = \sqrt{\frac{n_1^2 n_2^2}{f n_2^2 + (1-f) n_1^2}} \tag{2.1}$$

Where n_{TE} and n_{TM} are the effective indices for the TE and TM polarizations, f is the fill factor and n_1 and n_2 are the refractive indices of the grating. Unfortunately, the gratings being considered for this device are not sufficiently small for Equation 2.1 to provide a useful approximation. Rytov's[23] transcendental expressions, Equation 2.2, can be used in conjunction with a root-finding algorithm to determine a much better estimate of the effective indices for each polarization.

$$\frac{\sqrt{n_2^2 - n_{TE}^2}}{\mu_2} \tan\left[\left(\frac{\Lambda}{\lambda}\right)(1-f)\pi\sqrt{n_2^2 - n_{TE}^2}\right] = -\frac{\sqrt{n_1^2 - n_{TE}^2}}{\mu_1} \tan\left[\left(\frac{\Lambda}{\lambda}\right) f\pi\sqrt{n_1^2 - n_{TE}^2}\right] \tag{2.2}$$

Where Λ is the period of the grating, λ is the wavelength and μ_1 and μ_2 are the permeabilities of the grating materials. For n_{TM}, the permeabilities are replaced with the permittivities, ε. Alternatively, closed form approximations can be derived by using a series expansion of the tangent terms in Equation 2.2[24]. A second order expansion results in the expressions shown in Equation 2.3. Equation 2.3 provides a straightforward method for analyzing a design space that includes grating period, duty cycle and depth.

$$n_{TE}^{(2)} = \sqrt{\left(n_{TE}^{(0)}\right)^2 + \frac{\pi^2}{3}\left(\frac{\Lambda}{\lambda}\right)^2 f^2 (1-f)^2 \left(n_2^2 - n_1^2\right)}$$
$$n_{TM}^{(2)} = \sqrt{\left(n_{TM}^{(0)}\right)^2 + \frac{\pi^2}{3}\left(\frac{\Lambda}{\lambda}\right)^2 f^2 (1-f)^2 \left(n_2^2 - n_1^2\right) \frac{\left(n_{TE}^{(0)}\right)^2 \left(n_{TM}^{(0)}\right)^6}{n_1^4 n_2^4}} \tag{2.3}$$

Using Equation 2.2 or 2.3 to find the indices of the grating, candidate one dimensional gratings were found that minimized the divergence of the calculated phase retardance from the desired

value over the wavelength region of interest. These solutions were subsequently analyzed using RCWA and iteratively optimized.

The materials that were considered were limited to silicon and gallium arsenide. These materials have a high refractive index so the resulting birefringence is relatively large. This reduces the required etch depths easing fabrication requirements. Unfortunately, it also reduced the required lateral dimension to minimize losses to diffracted orders.

The dispersion of form birefringence helps provide an achromatic element over a limited spectral range; however, this element was designed for the wavelength region of 2 - 5 μm. A classic tradeoff emerged as candidate designs were evaluated. Gratings with subwavelength periods for the shortest wavelength had an achromatic phase retardance over a subset of the target spectral range. Gratings with better achromatic performance typically suffered from reduced transmission at shorter wavelengths due to power lost to diffraction orders within the substrate. The design effort resulted in a one dimensional grating with the parameters shown in Figure 2.2.

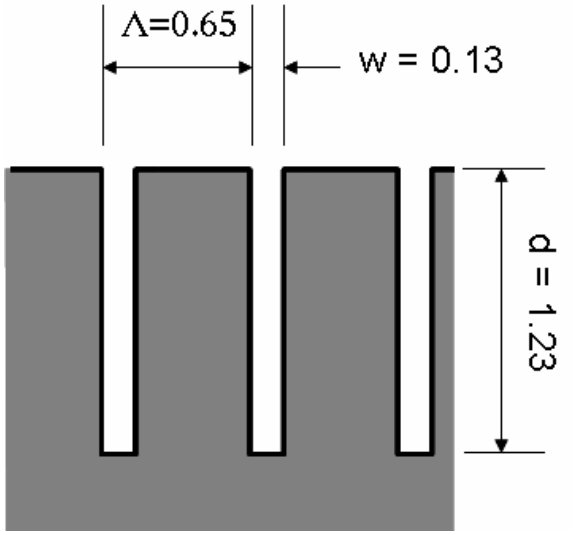

Figure 2.2 Target design for form birefringent quarter waveplate. The substrate is gallium arsenide and all dimensions are in microns.

The simulated performance of the nominal grating design is shown in Figure 2.3.

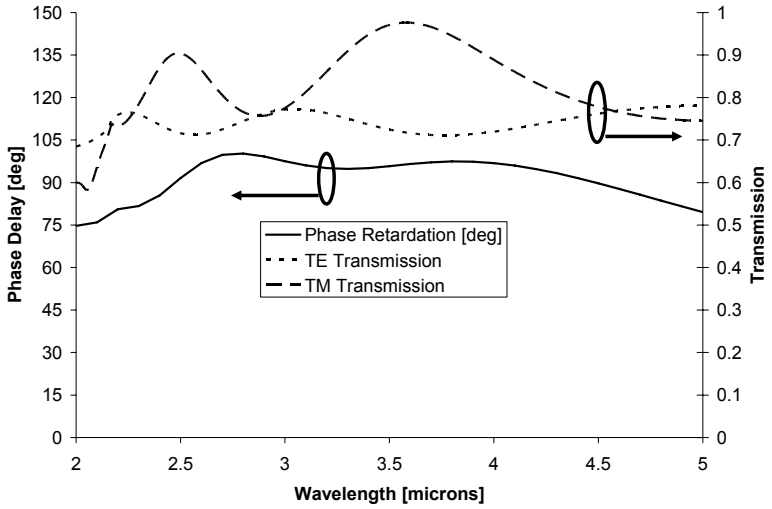

Figure 2.3 Simulated performance of form birefringent quarter waveplate.

Notice that the phase delay has good achromatic performance over the entire waveband with an average phase retardance of 91.3º and a peak to peak variation of 25.5º. The transmission efficiency shown is for the light entering the grating substrate. As will be shown later, an additional loss is incurred at the output interface of the gallium arsenide due to Fresnel reflections.

2.3 Fabrication

The fabrication process used an ebeam to define the lateral dimensions of the grating and chemically assisted ion beam etch (CAIBE) to etch the grating into the substrate. Figure 2.4 shows a simplified schematic of the fabrication process flow. A thin layer of SiO_2, approximately 30 nm thick, was deposited on the substrate first and followed by the ebeam photoresist, Figure 2.4 (a). The resist was exposed and developed where the grating would NOT be etched, Figure 2.4 (b). A metal layer comprised of titanium (20 nm) and nickel (120 nm) was then deposited to act as the etch mask, Figure 2.4 (c). A liftoff of the remaining ebeam resist patterned the metal etch mask appropriately. The exposed SiO_2 was then etched using a conventional RIE and opened the GaAs for the CAIBE, Figure 2.4 (d). The GaAs was etched using a chemistry comprised of Cl_2, BCl_3 and Ar, Figure 2.4 (e). The final process step was the removal of the etch mask. This was done by wet etching the SiO_2 underneath the remaining metal, Figure 2.4 (f).

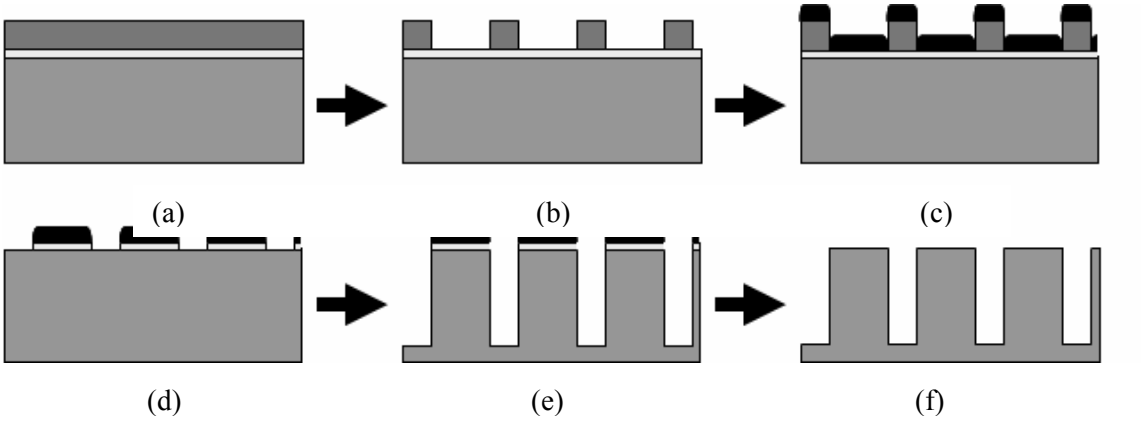

Figure 2.4 Basic process flow for fabrication of subwavelength grating in GaAs.

Test etches showed that the resulting duty cycle was approximately 5-10% smaller than desired, i.e. the fabricated trench width was wider then the target value. The two other basic parameters, period and etch depth, were reproduced with high accuracy. In addition, the side walls were excellent and the fabricated gratings provided a very close approximation to the rectangular groove shape assumed during the design process. Taking into account the reduced duty cycle, the actual devices were etched to a target depth of 1.0 μm rather than the design value of 1.23 μm. Figure 2.5 shows a SEM of a fabricated grating before the removal of the metal etch mask.

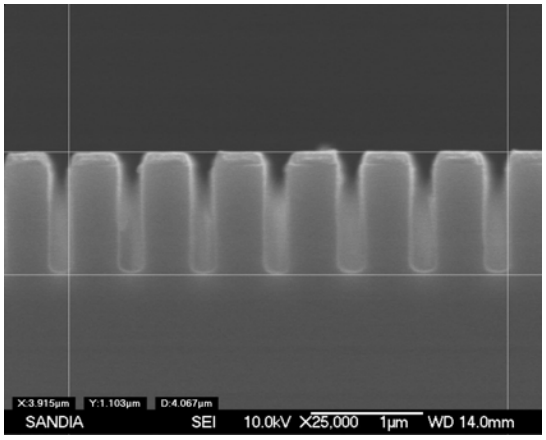

Figure 2.5 SEM of fabricated diffractive waveplate.

2.4 Experimental Measurement and Analysis

The fabricated parts were tested using the experimental arrangement shown schematically in Figure 2.6. A Glo-bar was used in conjunction with a monochromator to provide a tunable wavelength source. The output of the monochromator was collected with a CaF lens and directed through an IR polarizer. An iris was used to ensure that only the device was illuminated. The fabricated waveplate was mounted on a rotation stage to allow for measuring the output with respect to its angular position. An analyzing polarizer followed the waveplate and a final lens was used to focus the output on a MCT detector. A chopper was used at the input slit of the monochromator with the sync output sent to a lock-in amplifier. The lock-in

amplifier effectively removed the effects of dc background illumination and provided a high signal to noise ratio output.

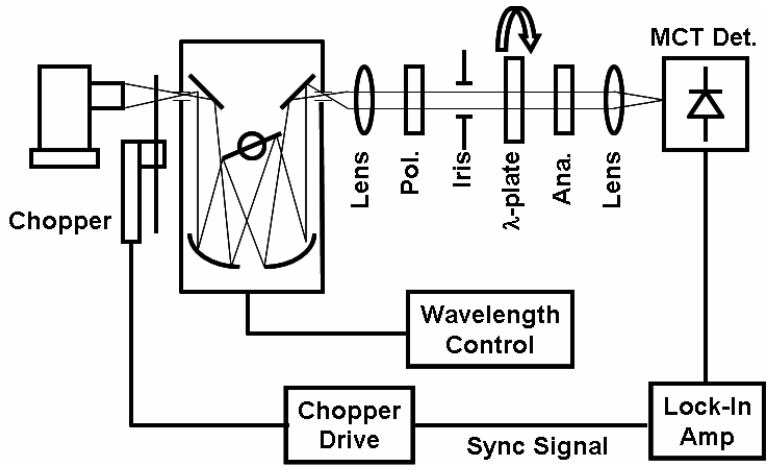

Figure 2.6 Schematic of test system used to determine phase delay of diffractive waveplate.

This system can be modeled using Jones matrices. Mueller matrices are often used for systems that are not fully polarized. While this is true for the Glo-bar source, the use of the first polarizer allows for the use of a simpler Jones matrix model. Equation 2.4 shows the basic model.

$$\begin{bmatrix} a_{out} \\ b_{out} \end{bmatrix} = \begin{bmatrix} b_{ana} & 0 \\ 0 & a_{ana} \end{bmatrix} \begin{bmatrix} \cos\theta & -\sin\theta \\ \sin\theta & \cos\theta \end{bmatrix} \begin{bmatrix} a_{wp} & 0 \\ 0 & b_{wp}\exp(i\phi_{wp}) \end{bmatrix} \begin{bmatrix} \cos\theta & \sin\theta \\ -\sin\theta & \cos\theta \end{bmatrix} \begin{bmatrix} a_{pol} & 0 \\ 0 & b_{pol} \end{bmatrix} \begin{bmatrix} a_{in} \\ b_{in} \end{bmatrix} \quad (2.4)$$

Where a and b are the horizontal and vertical polarizations, respectively, ϕ is the waveplate phase delay and θ is the rotation angle of the waveplate. The subscripts refer to the individual elements in the system; *pol* for the polarizer, *ana* for the analyzer and *wp* for the waveplate. In order to properly model the system, two alterations were made to Equation 2.4. First, a rotation was added to the analyzer to compensate for angular misalignment. Second, a small sinusoidal modulation of the input compensated for lateral misalignment of the waveplate. Since, the outputs of the Jones matrix model are field quantities, these results were squared to provide a value consistent with the intensity measurement made by the detector.

The output of the system was taken at several angular positions of the waveplate. In addition, the output of the system was measured without the analyzer in place. Theoretically, this would have provided no change with rotation of the waveplate; however, the fabricated part exhibited an appreciable amount of linear diattenuation at certain wavelengths. Linear diattenuators have a transmission efficiency that is dependent on the incident polarization[28]. This was expected from the simulated design results shown in Figure 2.3. Taking this additional data allowed for doing two simplified least-squares curve fits and provided a more stable analysis algorithm. In effect, the first curve fit determined the diattenuation parameters, a_{wp} and b_{wp}, and the second curve fit determined the phase retardation. Figure 2.7. displays an example of the two sets of data and the resulting curve fits.

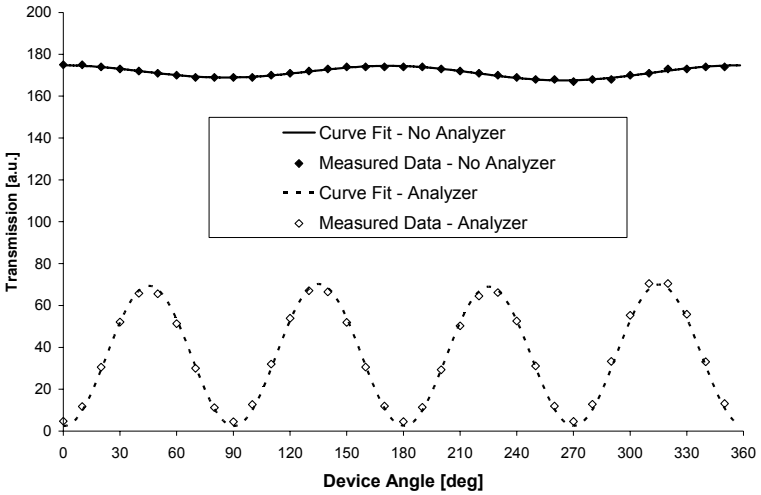

Figure 2.7 Example of data taken at 3.75 µm.

This process was repeated for several wavelengths across the spectral region of interest. The measured phase retardation is shown in Figure 2.8. along with the simulated response of the nominal design and the actual fabricated grating structure. Notice that the small error in the duty cycle caused a large change in the resulting phase delay, particularly at the longer wavelengths. The measured results had an average phase delay of 80.6º and a peak to peak variation of 30.8º. The simulated response of the fabricated grating had an average of 79.5º and total variation of 31.4º.

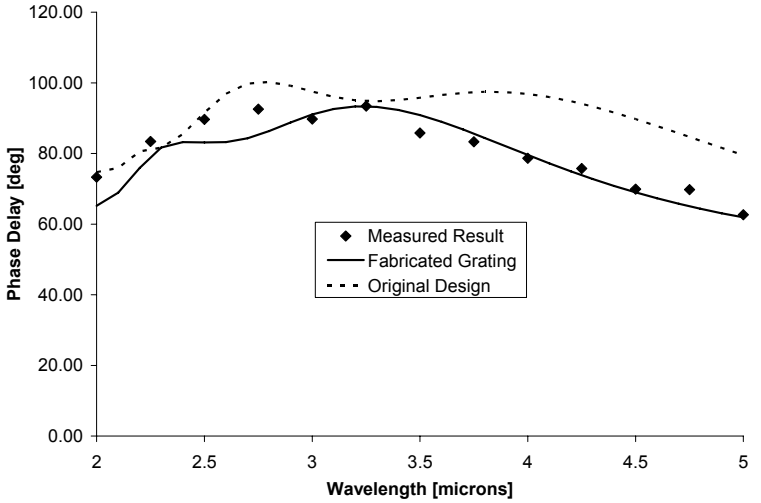

Figure 2.8 Comparison of measured phase delay of diffractive waveplate with simulated result based on fabricated grating and original design parameters.

The curve fit algorithm also determined the diattenuation parameters of the gratings. The values included the transmission efficiency of the grating and the losses due to Fresnel reflections at the backside of the device. Combining the Fresnel reflection with the simulated transmission efficiency of the grating results in the curves shown in Figure 2.9.

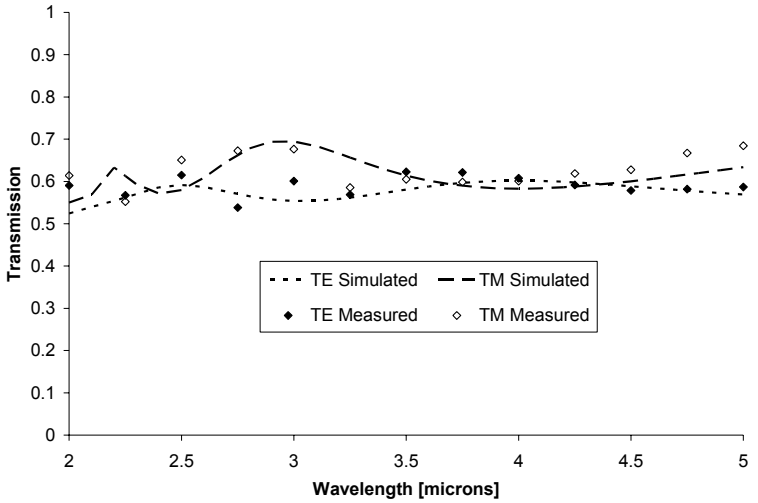

Figure 2.9 Simulated and measured TE and TM transmission of the diffractive waveplate. Fresnel losses are included.

One aspect of the fabricated gratings that effected the resulting measurements was an inconsistent removal of the metal etch mask. A small amount of the metal and a more substantial amount of the underlying SiO_2 was still present on the tested device. This led to some of the deviations between simulated and measured responses.

2.5 Finite Aperture Issues

One of the motivations for pursuing a diffractive waveplate is the ability to produce a spatially variant waveplate that can potentially be integrated with micropolarizer and detector arrays. Figure 2.10 shows a schematic layout of a "super-pixel" designed for an imaging polarimeter. The four detectors comprising the super-pixel would provide signals that could be used to determine all four Stokes vectors, as shown in Table 2.1. (An alternative approach uses a vertical polarizer over I_0.)

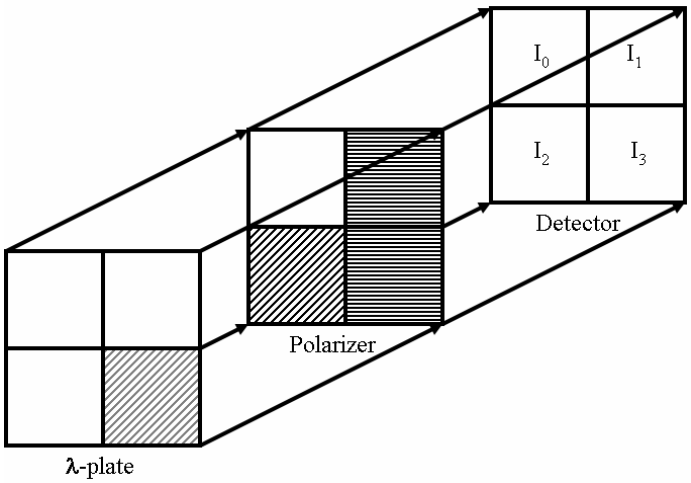

Figure 2.10 Layout of super-pixel utilizing pixilated waveplate for imaging polarimeter.

Pixel	λ/4-plate	Polarizer	Stokes Parameter
0	None	None	$S_0 = I_0$
1	None	Horizontal	$S_1 = 2*I_1-I_0$
2	None	45°	$S_2 = 2*I_2-I_0$
3	45°	Horizontal	$S_3 = 2*I_3-I_0$

Table 2.1 Super-pixel outputs and subsequent determination of Stokes parameters.

While the approach is intuitively appealing, the implementation presents several challenges. The most obvious is the use of small aperture sizes and the effects of propagation between elements. A typical focal plane array can have pixels as small as 15 μm. If the light has to propagate through the substrate of the diffractive waveplate, enough diffraction will occur to produce significant crosstalk between pixels. Figure 2.11 shows a simulated comparison between light propagating 0, 250 and 500 μm after passing through a periodic array of 30 μm pixels. The input was a horizontally polarized beam and the top row of images shows the horizontal portion of the image after the diffractive waveplate and the bottom row shows the vertical polarization. Immediately after the waveplate there is vertical polarization present only where the pixilated waveplate was present. Unfortunately, the periodic arrangement of small apertures leads to Talbot imaging resulting in the desired outputs appearing at the wrong pixels after a small propagation distance. After propagating an additional 250 μm, the outputs appear to be properly located over the appropriate pixels.

To avoid this type of diffraction, propagation distances would have to be smaller than 25 μm. Integrating both the diffractive waveplate and micropolarizer array with a focal plane array with this type of restriction is extremely challenging. Assuming each of these elements can be placed within such close proximity, near field effects may lead to interactions between the elements resulting in unexpected results and need to be examined in more detail. One alternative would be to use a spatial segregation of the image that uses much larger physical sizes.

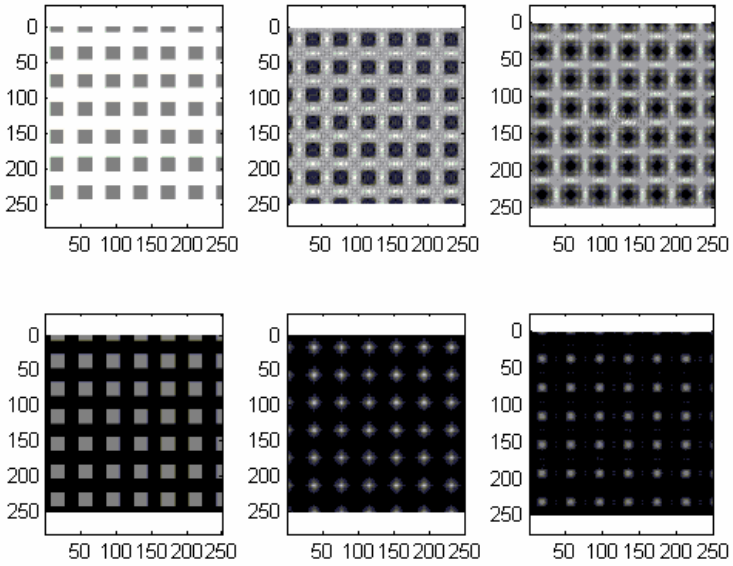

Figure 2.11 Output from pixilated waveplate with 30 mm pixels. The illuminating light had a wavelength of 3.5 μm and was horizontally polarized. The propagation distances were (a) 0 (b) 250 and (c) 500 μm.

2.6 Conclusions

The results presented here are an excellent initial attempt at fabricating an achromatic waveplate over the midwave IR spectral region. For substantially improved performance, there are possible paths that could prove fruitful. First, other suitable IR materials, such as InP or Si, may provide better achromatic performance; however, the increase in performance will most likely be limited. Second, a multilevel design would provide more parameters to aid the design of an achromatic waveplate[29]. Additionally, stacked gratings could help facilitate the incorporation of a diffractive waveplate with the other elements required for the polarimeter system[17]. Finally, a two dimensional grating design would also provide additional parameters that may prove useful in designing an achromatic element. Using the same design process outlined above would require a more complex determination of effective indices[30-32].

A design approach for an achromatic diffractive waveplate based on a one-dimensional subwavelength grating was presented. The use of effective medium theory and rigorous coupled wave analysis produced a design with good achromatic performance over the 2-5 μm spectral band. The fabrication process was discussed and the resulting device shown to be very close to the design target. Small errors in the duty cycle of the fabricated device led to significant changes in the performance with the measured part exhibiting a total variation of phase delay of 30.8º with an average delay of 80.6º.

3. Proximity Effects to Focal Plane Array

We are also interested in understanding the effects of a birefringent waveplate in proximity to wiregrid polarizers. Birefringent waveplate are usually fabricated in high refractive index substrates, while wiregrid polarizers are fabricated on top of low refractive index materials. For our case we are going to use gallium arsenide (GaAs) and fused silica (SiO_2). Using rigorous couple wave analysis (RCWA) it is possible to see some of the proximity effects on the extinction ratio of the wiregrid polarizer.

The analysis indicates variation in extinction ratio as the separation increases between the GaAs substrate and the wiregrid polarizer. See Figure 3 (a) for a basic schematic of the two devices. If using a bare GaAs substrate the extinction ratio oscillates as the wavelength increases. The oscillation frequency decreases as the separation between the two devices increases, see Figure 1.41 (b). Depositing an antireflective (AR) coating on the GaAs substrate reduces apparent the extinction ratio oscillation; see Figure 3 (c).

The AR coating should be patterned to the areas without gratings by lift-off method. Depositing an AR coating on the actual patterned areas of the GaAs substrate is unfeasible because the AR coating will change the optical characteristics of the grating. In addition, deposition rates can not be controlled well for vertical walls and sometimes deposition may not occur. Furthermore, the thickness of the AR coating could exceed the open lines of the grating. To solve this situation is desirable to fine tune the design of the grating with the wiregrid polarizer in proximity to the device.

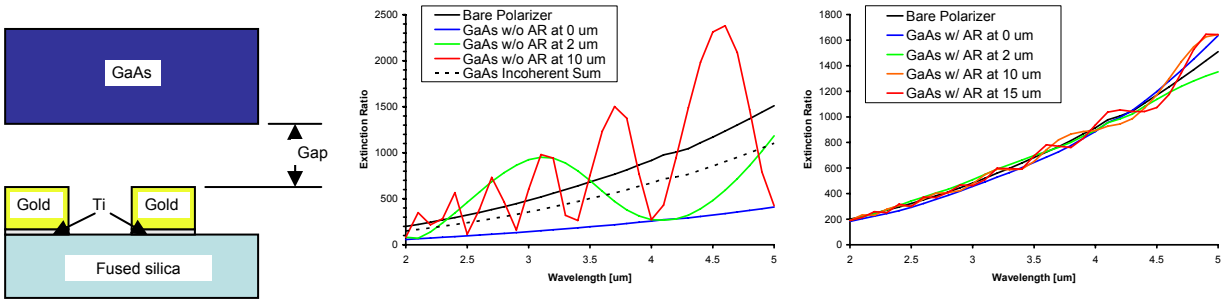

(a) (b) (c)

Figure 3. Depiction of a polarizer and birefringent waveplate proximity simulation (a) and the effect of not depositing (b) or depositing (c) an anti reflection coating on the non-patterned area of a pixelated birefringent waveplate in GaAs. Figure (b) shows a large variation in extinction ratio across the MWIR for different gaps, with the largest variation for the largest gap. Figure (c) indicates that a well designed AR coating on top of the pixelated waveplate reduces the variation on extinction ratio across the MWIR by a factor of 20.

4. Integrated Approach Proposal

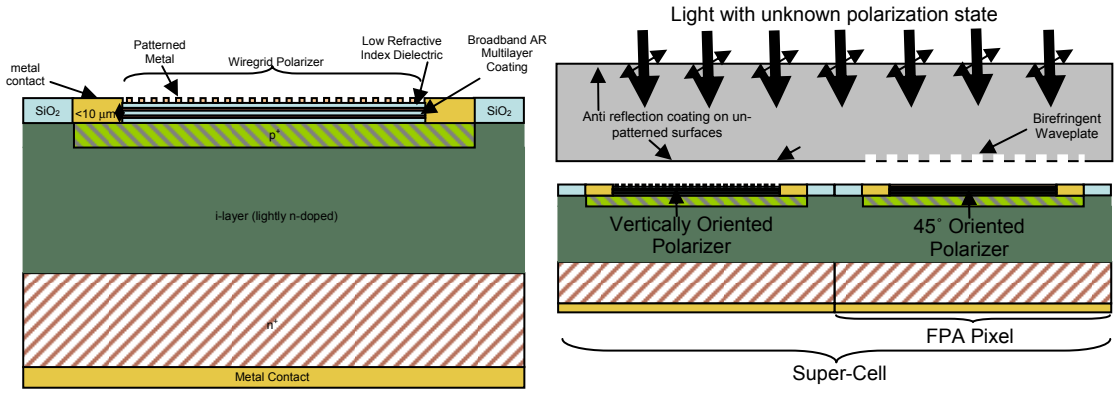

(a) (b)

Figure 4. Wiregrid polarizers are fabricated on top of the active areas on corresponding pixels of an FPA, Figure (a). An AR coating atop an FPA active area can reduce reflection from a low refractive index deposition and the metal (usually gold) wiregrids of the polarizer. For a full four Stokes parameter calculation a pixelated birefringent waveplate can be fabricated on an appropriate substrate and the patterned side oriented toward the FPA and aligned in close proximity to reduce cross-talk from diffraction, Figure (b).

Simulation and experimental data indicate that the performance of a super-pixel array, with pixel size between 15 to 20 µm, is affected by diffraction effects that induce cross-talk between adjacent pixels. This cross-talk occurs over gap distances less than 10 µm. It is expected that assembling of the pixelated birefringent-waveplate array and the polarizer super-pixel array will multiply the cross-talk issue given that both parts have pixelated structures and light has to propagate through some significant distance before incidence onto the FPA.

We propose[16] to monolithically integrate the micro-polarizer array to the FPA. Typically, the last step of an FPA fabrication process is the deposition of an anti-reflection (AR) coating. We suggest that the AR coating is tailored to meet the spectral reflection requirements with the deposition of a low refractive index dielectric last layer in mind. On top of the low refractive index layer a coating of gold, platinum or molybdenum is deposited and patterned to create the polarizer on top of each pixel. The wire patterns are aligned such that the super-pixel capture vertical, horizontal, full and circular polarization signals. The total distance between the polarizer and the active surface of the pixel is now less than 10 microns depending on the wavelength and the AR coating design. In addition, the technique used to fabricate the active area of the pixels in the FPA should provide a physical buffer between pixels; see Figure 4 (a).

The last step is to place the birefringent waveplate on top of the FPA-polarizer set, see Figure 4. (b). The distance between the two devices is now the glue distance, which usually is 10 µm. This is better than the option of placing the birefringent waveplate at least 400 µm away on top of the micropolarizer substrate. The 400 µm would be the minimal thickness for a low refractive index substrate.

Conclusions

The intent of this project was to demonstrate and verify components used in a snap shot polarimetric imaging system, the micropolarizer arrays and a wideband achromatic waveplates. We demonstrated that we can design, fabricate and test wiregrid polarizers and subwavelength achromatic waveplates to meet performance requirements of extinction ratio, transmitted signal and retardance.

Further work should be done in developing the fabrication of the wiregrid polarizer in lithium fluoride, but the results are promising. The same applies for the achromatic wave plate, which could benefit from the use of new materials like indium phosphide or silicon and even look at the use of new geometries to increase the band response.

We fabricated single isolated pixel-sized polarizers and characterized their extinction ratio, demonstrating that pixelated devices with sizes between 10 μm to 20 μm can have extinction ratios larger than 100:1. These results allow us to proceed with the fabrication and testing of several geometries for super-pixel arrays.

The results from testing micropolarizer super-pixel arrays indicate that fabricating each element (polarizer and waveplate) in its own substrate and stacking them is too sensitive to cross-talk. This cross-talk is the product of diffraction from the periodic structures defined by the pixelated micropolarizers and/or micro-waveplates. The diffracted light bleeds into adjacent pixels as the light propagates inside the substrate of the next element or into free space. The main concern is that contributions from polarization states with the incorrect polarization alignment will indicate the presence of nonexistent targets by bleeding into a pixel that is supposed to be black. This could lead to a false-positive target in the polarimetric image.

Increasing the dimension of the pixel sizes will alleviate the cross-talk problems. This approach goes in the wrong direction if the number of pixels in the FPA exceeds a 1 million (1024 by 1024) pixels. In addition alignment and material issues may creep between the different materials used for each component. To further reduce cross talk, the active area of each pixel in the FPA should be reduced a good percentage from the actual size of the pixel, allowing the stop of undesirable light into the active area. However, this also degrades the signal-to-noise ratio.

An integrated approach will provide a better alternative in the long run. In this case the polarizers are monolithically integrated to FPA as part of the fabrication process of the device. The birefringent waveplate is fabricated in its own substrate and aligned with the grating facing the FPA-polarizer active area. The waveplate should have AR coatings on both sides of the substrate. The side with the grating should be patterned so the AR coating is not deposited on top of the grating. This approach implies modifications to the typical FPA fabrication process.

References

1. O. Matoba and B. Javidi, "Three-dimensional polarimetric integral imaging," Opt. Lett., **29**, 2375-2377, 2004.

2. J. Peterson, G. L. Jensen, J. A. Kristi, and J. A. Shaw, "Polarimetric imaging using continuously spinning polarizer element," Proc. SPIE, **4133**, 292-300, 2000.

3. D. S. Sabatke, A. M. Locke, M. R. Descour, W. C. Sweatt, J. P. Garcia, E. L. Dereniak, S. A. Kemme, G. S. Phipps, "Figures of merit for complete Stokes polarimeter optimization," Proc. SPIE, **4133**, 75-81, 2000.

4. D. S. Sabatke, M. R. Descour, E. L. Dereniak, W. C. Sweatt, S. A. Kemme, G. S. Phipps, "Optimization of retardance for complete Stokes polarimeter," Opt. Lett., **25**, 802-804, 2000.

5. G. P. Nordin, J. T. Meier, P. C. Deguzman and M. W. Jones, "Micropolarizer array for infrared imaging polarimetry," J. Opt. Soc. Am. A., **16**, 1168-1174, 1999.

6. J. Guo and D. J. Brady, "Fabrication of high-resolution micropolarizer arrays," Opt. Eng., 36, 2268-2271, 1997.

7. J. Guo and D. J. Brady, "Fabrication of thin-film micropolarizer arrays for visible imaging polarimetry," App. Opt., **39**, 1486-1492, 2000.

8. R. R. Boye, S. A. Kemme, J. R. Wendt, A. A. Cruz-Cabrera, G. A. Vawter, C. R. Alford, T. R. Carter, S. Samora, "Pixilated Wideband Achromatic Waveplates Fabricated for the Mid IR Using Subwavelength Features," Proc. of SPIE, **6127**, p. 612709-1-10, 2006.

9. A. A. Cruz-Cabrera, S. A. Kemme, J. R. Wendt, R. R. Boye, T. R. Carter, S. Samora, "Edge Termination Effects on Finite Aperture Polarizers for Polarimetric Imaging Applications at Mid Wave IR," Proc. of SPIE, **6126**, p. 61260K-1-10, 2006.

10. M. Born and E. Wolf, *Principle of Optics*, 554-555, Pergamon Press, Oxford, 1991.

11. H. Hertz, *Electric Waves*. London: Macmillan Company, Ltd., 1983.

12. M. G. Moharam and T. K. Gaylord, ''Rigorous coupled-wave analysis of metallic surface-relief gratings,'' J. Opt. Soc. Am. A **3**, 1780–1787, 1986.

13. M. A. Jensen and G. P. Nordin, "Characterization of two-dimensional finite-aperture wire grid polarizers by a spectral-domain technique," Appl. Opt., **40**, 4738-4745, 2001.

14. M. A. Jensen and G. P. Nordin, "Finite-aperture wire grid polarizers," J. Opt. Soc. Am. A, **17**, 2191-2198, 2000.

15. G. P. Nordin, J. T. Meier, P. C. Deguzman, and M. W. Jones, "Diffractive Optical Element for Stokes Vector Measurement With a Focal Plane Array," SPIE, **3754**, 169-177, 1999.

16. A. A. Cruz-Cabrera, S. A. Kemme, R. R. Boye, Technical Advance: *Monolithically Integrated Wire Grid Polarizer to Focal Plane Array*, SD: 10313, 2006.

17. P. C. Deguzman and G. P. Nordin, "Stacked subwavelength gratings as circular polarization filters," App. Opt., **40**, 5731-5737, 2001.

18. H. Kikuta, Y. Ohira and K. Iwata, "Achromatic quarter-wave plates using the dispersion of form birefringence," App. Opt., **36**, 1566-1572, 1997.

19. G. P. Nordin and P. C. Deguzman, "Broadband form birefringent quarter-wave plate for the mid-infrared wavelength region," Opt. Express, **5**, No. 8, 163-168, 1999.

20. N. Bokor, R. Shechter, N. Davidson, A. A. Friesem and E. Hasman, "Achromatic phase retarder by slanted illumination of a dielectric grating with period comparable with the wavelength," App. Opt., **40**, 2076-2080, 2001.

21. Y. Deer, T. Qiaofeng, L. Haitao, Y. Yingbai and J. Guofan, "An achromatic quarterwave-plate for visible spectrum region using the dispersion of form birefringence," Proc. SPIE, **4924**, 9-13, 2002.

22. D. Yi, Y. Yan, H. Liu, S. Lu, G. Jin, "Broadband achromatic phase retarder by subwavelength grating," Optics Commun, **227**, 49-55, 2002.

23. S. M. Rytov, "Electromagnetic properties of a finely stratified medium," Sov. Phys. JETP, **2**, 466-475, 1956.

24. D. H. Raguin and G. M. Morris, "Antireflection structured surfaces for the infrared spectral region," App. Opt., **32**, 1154-1167, 1993.

25. C. W. Haggans, L. Li and R. K. Kostuk, "Effective-medium theory of zeroth-order lamellar gratings in conical mountings," J. Opt. Soc. Am. A, **10**, No. 10, 2217-2225, 1993.

26. M. G. Moharam, E. B. Grann, D. A. Pommet and T. K. Gaylord, "Formulation for stable and efficient implementation of the rigorous coupled-wave analysis of binary gratings," JOSA A, **12**, 1068-1076, 1995.

27. M. G. Moharam, E. B. Grann, D. A. Pommet and T. K. Gaylord, "Stable implementation of the rigorous coupled-wave analysis for surface relief gratings: enhanced transmittance matrix approach," JOSA A, **12**, 1077-1086, 1995.

28. R. A. Chipman, "Polarimetry," *Handbook of Optics, Vol. 2*, 2nd ed., M. Bass ed., McGraw-Hill, New York, NY, 1995.

29. W. Yu, H. Kikuta and T. Konishi, "Synthesis of polarization-selective optical components with multi-layer subwavelength structures," Proc. SPIE, **5183**, 184-191, 2003.

30. E. B. Grann, M. G. Moharam and D. A. Pommet, "Artificial uniaxial and biaxial dielectrics with use of two-dimensional subwavelength binary gratings," JOSA A, **11**, No. 10, 2695-2703, 1994.

31. H. Kikuta, Y. Ohira, H. Kubo and K. Iwata, "Effective medium theory of two-dimensional subwavelength gratings in the non-quasi-static limit," JOSA A, **15**, No. 6, 1577-1585, 1998.

32. M. S. Mirotznik, D. M. Putsai, D. W. Prather and J. N. Mait, "Design of two-dimensional polarization selective diffractive optical elements with form-birefringent microstructures," Appl. Opt., **43**, 5947-5954, 2004.

Distribution

2	MS 1082	Shanalyn Kemme, 1725
5	MS 1082	Alvaro Cruz-Cabrera, 1725
1	MS 1082	Robert Boye, 1725
1	MS 1082	Jim Hudgens, 1725
1	MS 1082	Joel Wendt, 1725
1	MS 1082	Tony Carter, 1725
1	MS 1082	Sally Samora, 1725
1	MS 1085	Gregory Vawter, 1742
1	MS 1085	Chuck Alford, 1742
1	MS 1085	Charles Sullivan, 1724
1	MS 0406	Jody Smith, 5751
1	MS 0406	Prabal Nandy, 5712
1	MS 0980	Stephen Gentry, 5703
2	MS 9018	Central Technical Files, 8944
2	MS 0899	Technical Library, 4536
1	MS 0123	Donna Chavez, LDRD Office, 1011